STAR NOTE

Simulation of Detector Performance and Analysis of the Physics Capabilities of STAR

Dan Cebra,[a] Bill Christie,[b] Jim Draper,[a] Wen Gong,[c] Mike Lisa,[c]
Ricardo Mastroleo,[d] Jeffery Mitchell,[b,c] Stathes Paganis,[d]
Sanjeev Pandey,[e] Lanny Ray,[d] Konstantin Shestermanov,[b,f]
and Pablo Yepes[g]

Edited by Lanny Ray

June 1995

[a] Dept. of Physics, Univ. of California at Davis
[b] Physics Dept., Brookhaven National Laboratory
[c] Nuclear Science Division, Lawrence Berkeley Laboratory
[d] Dept. of Physics, Univ. of Texas at Austin
[e] Dept. of Physics, Ohio State Univ.
[f] Institute of High Energy Physics, Protvino, Russia
[g] Bonner Nuclear Laboratory, Rice University

Abstract

Simulation results for the STAR time projection chamber (TPC), time-of-flight (TOF), and external time projection chamber (XTPC) detectors are presented and discussed which demonstrate their performance capabilities with respect to tracking, particle identification and charge identification. Integrated tracking performance for the combined silicon vertex tracker (SVT) and TPC is also discussed. Results of Monte Carlo simulation studies are presented for some of the physics issues addressed by STAR. These physics topics include: (1) global, event-by-event characterization of nucleus-nucleus central collisions, (2) jet production, (3) high p_T particle production, (4) physics at high pseudorapidity ($|\eta| > 2$), and (5) two-particle correlation studies of source sizes. The results presented here are, of course, dependent on the current status of the simulation and analysis software for STAR. Significant improvements were made during 1994 in the TPC detector simulation software and the event reconstruction analysis software. The present results provide a reasonable, first estimation of the eventual performance and physics analysis capabilities of STAR using analysis modules and data structures which operate strictly within the STAR off-line analysis shell.

Contents

1 Introduction

At the January 1995 STAR Collaboration meeting the Simulations and Analysis Software (SAS) group presented results of simulations during a one day plenary session. The simulation results demonstrated the performance of each subdetector (TPC, SVT, TOF, EMC, XTPC and trigger) as well as the overall performance of STAR with respect to tracking, particle identification (PID), neutral and total energy detection, jet finding, triggering, etc. The simulations were also designed to investigate the capability of STAR to achieve the many, varied physics goals which together comprise the mission of STAR. Included in these presentations were studies of STAR's ability to (1) trigger on selected, interesting classes of events, (2) observe event-by-event fluctuations by measuring global properties of the collision (*e.g.* multiplicity, temperature, mean p_T, particle production ratios) for single events, (3) observe strangeness enhancement and anomalous particle production ratios by detecting and identifying singly and multiply strange baryons and mesons, (4) observe jet quenching or anomalous jet production, (5) measure gluon structure functions in nuclei by detecting and measuring jet-jet and γ-jet production in $p+p$, $p+A$ and $A+A$ collisions, (6) observe and measure charm production and other very short lived states (*e.g.* ϕ-mesons), (7) study possible temperature variations with pseudorapidity, η, baryon stopping and flow by measuring multiplicities at high $\mid \eta \mid > 2$, (8) observe source sizes via two particle correlations for identical bosons, both for single events and inclusively, and (9) observe anomalous, enhanced particle production at low p_T, which might indicate $q\bar{q}$ chiral condensation effects in a quark-gluon plasma (QGP), using the SVT. Most of these simulation projects are included in this Starnote.

The results presented here represent the status of the detector simulation and event reconstruction analysis software as of the January 1995 Star collaboration meeting. Sufficient progress occurred in the STAR off-line simulation and analysis software during 1994 to warrant the present documentation effort. Realistic detector simulation, cluster finding and hit reconstruction software for the TPC was well underway by the end of 1994. A comprehensive event reconstruction analysis chain had been completed and tested for *single* Au + Au events which included (1) SVT and TPC tracking, (2) SVT-TPC track-to-track matching, (3) global track refitting, (4) primary vertex location, (5) particle identification using dE/dx in the SVT and TPC, (6) secondary vertex identification and neutral parent track determination, (7) electromagnetic energy and neutral hadronic energy detection, and (8) extrapolation of reconstructed tracks back to the primary vertex with summary listing of primary particles. The TOF PID modules and the XTPC tracking were operational in the STAR analysis shell (TAS), however due to technical problems these modules were not functioning within the analysis chain at the time these simulations were done. (These limitations have, or soon will be, eliminated). Much software developement and testing remains to be done by the SAS group, but the results presented here are of sufficient quality to indicate the kinds of physics issues which STAR will be capable of addressing in the future as well as the quality of the information which STAR should be able to obtain. The SAS group believes that these results, although preliminary, will be useful to the STAR collaboration as a whole.

Detector performance simulations are presented and discussed in Sec. II of this document. This includes the TPC detector/electronics/DAQ simulator, TPC cluster/hit finder, TOF particle identification, XTPC tracking, and combined SVT-TPC tracking and momentum/position resolution studies. Physics analysis simulation results are presented and discussed in Sec. III. These include event-by-event analyses, jet finding, high p_T processes, physics at $|\eta| > 2$, and source size determination via HBT correlations. The figures are located in each subsection while the references are collected at the end of the document.

2 Simulations of Detector Performance

The purposes for simulating detector performance are: (1) to assist in making design choices, (2) to assist in the development of trigger, data acquisition (DAQ) and off-line event reconstruction software by providing simulated, raw data, and (3) to provide the necessary tools for studying detector acceptances and efficiencies.

2.1 The STAR-TPC Slow Simulator

Contributed by: Wen G. Gong

Introduction

The STAR-TPC slow simulator computes the response of a gas filled, time-projection-chamber (TPC) to the passage of ionizing particles which leave behind an ionization trail. The STAR TPC slow simulator provides the necessary tools to: (1) evaluate spatial resolution and two-track separation, (2) optimize algorithms for cluster-finding and tracking, (3) test data compression for the design of the Data Acquisition System, and (4) function as an experimental filter for comparing model predictions with experimental data. A fast TPC simulator [1] has been used so far for most physics simulations. It is computationally efficient, but lacks many physical considerations and an algorithm for cluster reconstruction. Implementation of a slow simulator together with a hit finder will provide a more realistic analysis chain for physics simulations. More details about this slow simulator are presented in Ref. [2].

Model for the Slow Simulator

An event generator produces particle tracks in a nucleus-nucleus collision. Electron clusters along charged particle tracks are generated by GEANT in the TPC volume. Each cluster corresponds to a track segment of a few millimeters (in the direction perpendicular to anode wires). The number of electrons (n_e) is calculated by the ratio of energy loss (ΔE) to the average ionization potential (aip) of the gas mixture. This cluster of electrons is transported in a uniform electrical drift field from a space point to the sense wire plane. Both longitudinal and transverse diffusions are considered for the electron cloud. Gas gain fluctuation is incorporated according to the Polya function. After the avalanche, charges are spread over close-by pads in accordance with the measured pad response functions. The shaper response is folded with the longitudinally diffused cluster along the drift time. The signal amplitude is sampled at the switched capacitor array (SCA) clock frequency. The shaper-filtered white noise is added to the signal at each time bucket for every pad affected. All the signals, pixel by pixel, are finally digitized to ADC counts once they are over a preset threshold level. Those ADC values with associated identifications of pad and time bucket are packed in a compact format for the

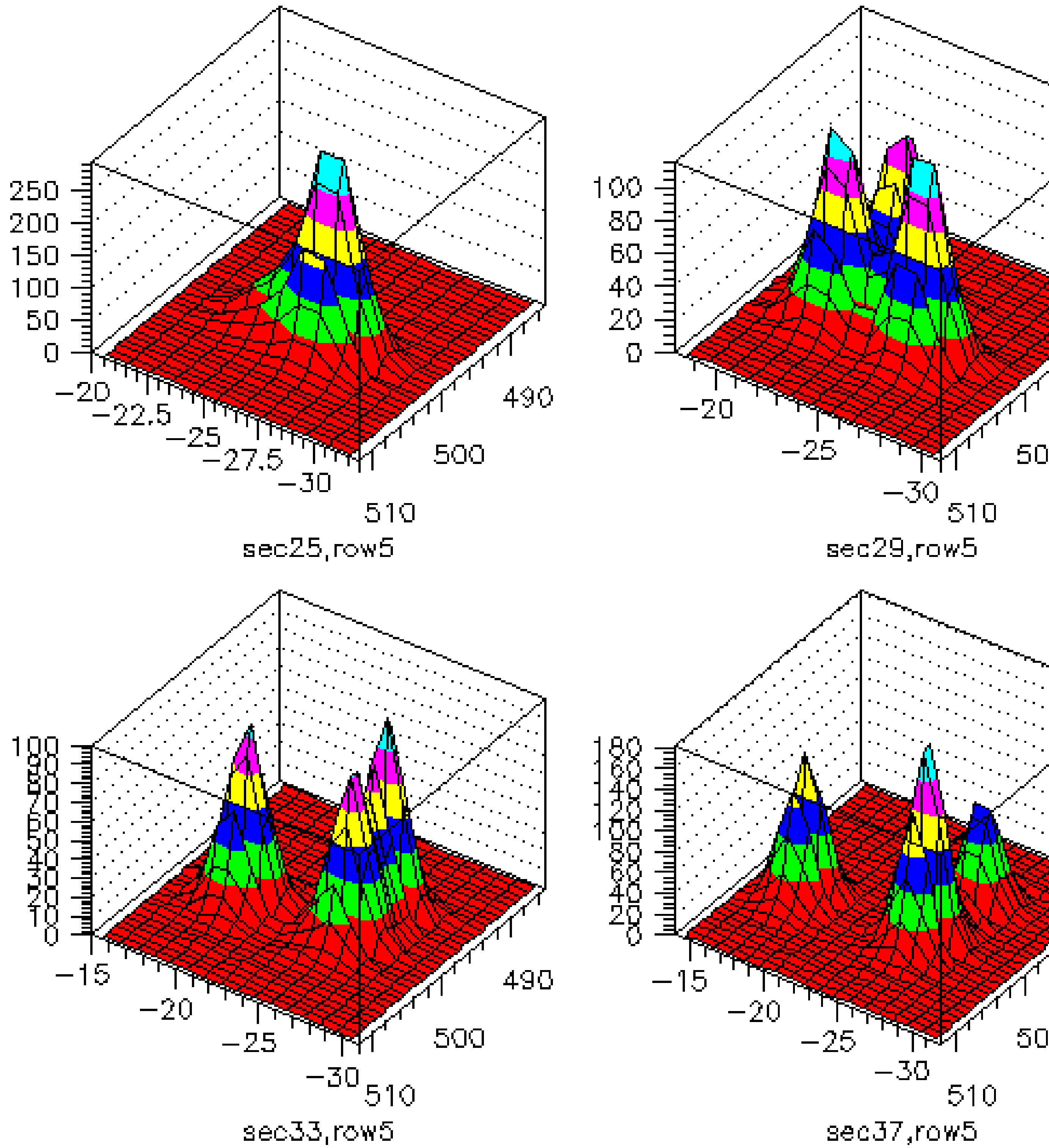

Figure 1: Pulse height spectrum versus pad number and time bucket for row 5 of inner sectors.

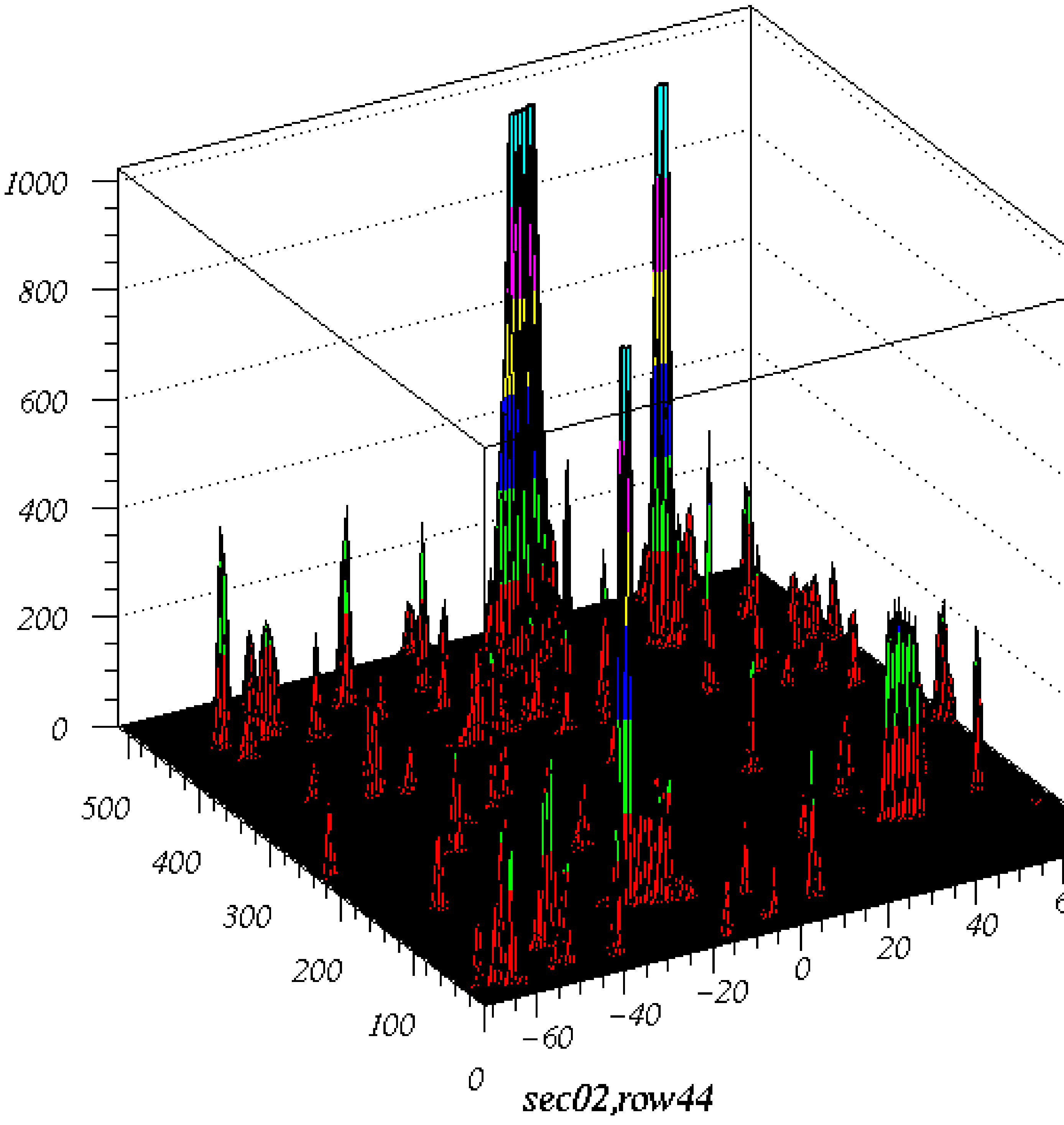

Figure 2: Pixel data output for row 44 of sector #2 from one Au+Au collision event.

simulator output.

In the following we give analytic expressions used in the STAR-TPC slow simulator. These are implemented in package *tss* in the STAR software library. This package was first prototyped by R. Morse [3], based upon subroutines provided by D. Roehrich and M. Levine [4]. However, it was much revised and improved in this work [2]. The pad response function along a pad row was corrected, and the measured shaper response function was used. The pad response function across a pad row, avalanche gain fluctuation, and shaper-filtered white noise are all new features added in this work.

Pad Response

Assuming a charged cluster originated at a space point $(x_0,\ y_0,\ z_0)$, the pad response function along the anode wire (or along the pad row) is a convolution of the transverse diffusion function with the pad response function (prf), where

$$F(x_p, x_0) = \int_{-\infty}^{\infty} dx' \frac{\exp[-\frac{(x'-x_p)^2}{2\sigma_{prf}^2}]}{\sqrt{2\pi}\sigma_{prf}} \cdot \frac{\exp[-\frac{(x_0-x')^2}{2\sigma_t(z_0)^2}]}{\sqrt{2\pi}\sigma_t(z_0)} = \frac{\exp[-\frac{(x_0-x_p)^2}{2(\sigma_{prf}{}^2+\sigma_t(z_0)^2)}]}{\sqrt{2\pi}\sqrt{\sigma_{prf}{}^2+\sigma_t(z_0)^2}}\ , \quad (1)$$

$\sigma_t(z_0) = \sigma_t \cdot \sqrt{z_0}$, and σ_t is the transverse diffusion constant.

For the pad response across the anode wire, the pad response function is not a gaussian, but rather a sum of step functions defined by the wire positions. This pad response function $f(y)$ is parametrized as:

$$f(y) = \varepsilon_1\Phi(y_1-|y|)+\varepsilon_2[1-\Phi(y_1-|y|)]\Phi(y_2-|y|)+\varepsilon_3[1-\Phi(y_2-|y|)]\Phi(y_3-|y|) \quad (2)$$

where $\varepsilon_1 = 100\%$, $\varepsilon_2 = 50\%$, and $\varepsilon_3 = 5\%$. $\Phi(y) = 1$ (if $y \geq 0$), and 0 (if $y < 0$). For an outer sector, $y_1 = 0.8cm$, $y_2 = 1.2cm$, and $y_3 = 1.6cm$. For an inner sector, $y_1 = 0.4cm$, $y_2 = 0.8cm$, and $y_3 = 1.2cm$. The convolution with the transversely diffused cluster gives

$$F(y_p, y_0) = \int_{-\infty}^{\infty} dy' f(y'-y_p) \frac{\exp[-\frac{(y_0-y')^2}{2\sigma_t(z_0)^2}]}{\sqrt{2\pi}\sigma_t(z_0)} \quad (3)$$

$$F(y_p, y_0) = \frac{1}{2}[(\varepsilon_1-\varepsilon_2)\cdot\Delta erf(y_0, y_p, y_1)+(\varepsilon_2-\varepsilon_3)\cdot\Delta erf(y_0, y_p, y_2)+\varepsilon_3\cdot\Delta erf(y_0, y_p, y_3)] \quad (4)$$

where $\Delta erf(y_0, y_p, y_i) \equiv erf(\frac{y_0-y_p+y_i}{\sqrt{2}\sigma_t(z_0)}) - erf(\frac{y_0-y_p-y_i}{\sqrt{2}\sigma_t(z_0)})$ for i=1,2,3, and $erf(y)$ is the error function. (x_p, y_p) is the center of a pad.

Shaper Response

Along the drift (time) direction, the response is a convolution of the shaper response function with a longitudinally diffused cluster. The shaper response function for one-stage differentiation and two-stage integration RC-CR shaper is

$$g(t,\tau) = \Phi(t)(\frac{t}{\tau})^2\exp(-\frac{t}{\tau}). \quad (5)$$

The shaper response is then

$$F(t,t_z) = \int_{-\infty}^{\infty} dt' g(t-t',\tau) \frac{\exp[-\frac{(t'-t_z)^2}{2\sigma_l(z_0)^2}]}{\sqrt{2\pi}\sigma_l(z_0)} \tag{6}$$

$$F(t,t_z) = (\frac{\sigma_l(z_0)}{\tau})^2 \cdot \exp[\frac{\sigma_l(z_0)}{\tau}(\lambda - \frac{\sigma_l(z_0)}{2\tau})] \cdot [\frac{1+\lambda^2}{2}(1-erf(\frac{\lambda}{\sqrt{2}})) - \frac{\lambda}{\sqrt{2\pi}}\exp(-\frac{\lambda^2}{2})] \tag{7}$$

where $\lambda = \frac{t_z - t}{\sigma_l(z_0)} + \frac{\sigma_l(z_0)}{\tau}$, $t_z = \frac{z_0}{v_d}$, and v_d is the drift velocity.

Gain Fluctuation

Given an average gain G_0, the avalanche gain fluctuation follows the Polya distribution.

$$P(m) = \frac{m(mG/G_0)^{m-1}}{\Gamma(m)} \cdot \exp(-mG/G_0) \tag{8}$$

where typically $m = 1.5$ for a multiwire proportional counter. This distribution is sampled between $G/G_0 = 0.1$ to 2.1 to generate the gas gain G.

Filtered White-Noise

Since a shaper is usually band-width limited, white noise on the pad will appear less "white" to the SCA. To include noise in the pixel data, we add the shaper-filtered white-noise spectrum after being renormalized to an Equivalent-Noise-Charge (ENC) value measured by the front end electronics. In the frequency domain, the power spectrum density for white noise is independent of frequency, but the phase of the white-noise amplitude is undetermined. We choose this phase to be random [5]. The convolution of white-noise amplitude and the shaper response function in the time domain can be computed using the Fast Fourier Transform(FFT), where

$$N(t) = \frac{1}{\mathsf{N}} \mathsf{FFT}^{-1}[\exp(-i\phi) * \mathsf{FFT}\{g(t,\tau)\}] \tag{9}$$

where $\phi = 2\pi \cdot RNDM()$ is the random phase, and N is the renormalization constant so that $N(t)$ will have a RMS equivalent to the ENC for the front end electronics.

Putting everything together, we get the signal (in terms of electrons) for one pixel as follows:

$$S(x_p, y_p, t) = n_e \cdot G \cdot F(x_p, x_0) \cdot F(y_p, y_0) \cdot F(t, t_z) + N(t). \tag{10}$$

Two-track Separation

To study two-track separation capability of the STAR-TPC, we generated three close tracks within each sector corresponding to pions of $p_T = 1.0$ GeV/c, $\eta = 0.1(\theta = 84.3^o)$. The track separations were set by $\Delta\theta = \Delta\phi = 0.5^o \cdot n$ where $n = 1, 2, ..., 6$. After running GEANT to produce hits in the TPC volume, we ran the TPC Slow Simulator (*tss*) to generate pixel data. Fig. 1 shows three dimensional plots of pulse height vs. pad number and time bucket on row #5 of an inner sector. Four sectors were chosen with $\Delta\theta = \Delta\phi$ ranging from 0.5^o to 2.0^o. Plots for other padrows at inner and outer sectors were similar. We find that two tracks with separation of $\Delta\theta = \Delta\phi \approx 1.0^o$ can be resolved by a hit-finder with a simple deconvolution algorithm. Two tracks at closer separation may be possible to resolve with better deconvolution techniques. This result is actually consistent with a simple estimate by $3 \times w_{pad}$ separation between tracks when the induced signal from each track spreads over 3 pad widths (w_{pad}). For example, $\Delta\phi = \tan^{-1}(\frac{3\times 3.35mm}{600mm}) = 0.96^o$, for the first padrow of an inner sector; and $\Delta\phi = \tan^{-1}(\frac{3\times 6.67mm}{1271mm}) = 0.91^o$, for the first padrow of an outer sector.

One Au+Au Collision Event

One HIJING event for Au+Au central collision at E/A = 200 GeV was used for our initial data analysis. A total of 705000 hits were generated by GEANT. A total of 9 million pixel data were produced by the slow simulator (*tss*). This corresponded to an occupancy of 13% on average. Difficulty arose when this large volume of data was handled by Zebra. Fortunately, a new data format (XDF) has been implemented by C. Tull, W. Greiman, and D. Olson which overcomes this limitation of the Zebra data format. The new data format is necessary for processing Au+Au collision events in the TAS environment. Fig. 2 displays a plot of pulse height spectrum vs. pad number and time bucket for row 44 in an outer sector. This pixel data would next be processed by another analysis package which does hit reconstruction.

Summary

We have implemented a slow simulator for the STAR-TPC (*tss*). This version of the slow simulator corrected previous treatments of the pad response and shaper response. It also added new features such as pad response across anode wires, gas gain fluctuation, and shaper-filtered white-noise. We have studied two-track separation capability of the STAR-TPC which is around $\Delta\phi \approx \Delta\theta \approx 1.0^o$. We have processed one Au + Au collision event at E/A = 200 GeV and provided pixel data ready for hit-reconstruction. The average pixel occupancy was about 13%.

Helpful discussions with Howard Wieman on pad/shaper response functions and the filtered-white-noise, with Mike Lisa on debugging the previous version of the slow simulator, and with Iwona Sakrejda on running GEANT are acknowledged. Thanks is also given to Doug Olson and Craig Tull for help with TAS-related problems and for implementing the new data format (XDF).

2.2 Cluster Finder and Space Point Reconstruction in STAR-TPC

Contributed by: Mike Lisa

Introduction

Cluster-finding and space-point reconstruction in the STAR TPC is the job of the *tcl* package. The active volume of the TPC is divided into 70 million pixels by the front-end electronics (or slow simulator), which converts the ionization charge into "raw" ADC data (that has been gain/pedestal corrected and zero-suppressed). The *tcl* software converts this data into a series of space-points (often called "hits") that correspond to points along trajectories of charged particles through the TPC. These points are passed to the tracking software, which links them into tracks.

Since space-point reconstruction is the earliest data reduction step, its performance will strongly affect the overall performance of the particle reconstruction analysis chain. Identification of true ionization clusters, rejection of false (noise) clusters, and accurate determination of ionization charge will affect particle identification and track-finding capabilities, while accurate extraction of spatial information, including uncertainties, is critical for momentum resolution and track segment matching. Finally, the ability to separate overlapping clusters at this early stage will have significant impact on HBT studies and secondary vertex searches.

The *tcl* package is currently at the beginning of its development. The mechanics of space-point reconstruction are in place, and slow simulator data on sparse events has been processed. A general description of the current method of space-point extraction and first results are given below.

Analysis Modules

The *tcl* package consists of two analysis modules: *tcl*, which identifies clusters of ionization in the two-dimensional time-bucket-versus-pad space for each padrow, and *tph*, which acts on these clusters to extract spatial information, and deconvolute multi-peak clusters.

The cluster-finder, *tcl*, first looks in the time direction for each pad to identify *sequences* on each pad, defined as consecutive time buckets with ADC values over threshold (set by *tss* or front-end electronics). Then, it looks in the pad direction for sequences which overlap in time and which are on adjacent pads. Especially for high track densities, a cluster found by *tcl* has its origin in several GEANT tracks. Fig. 3 plots time bucket vs pad number for an inner padrow in a low-noise sparse event. Occupied pixels (above threshold) are shown as dark points, and clusters identified by *tcl* are circled. To reduce false cluster identification, single-sequence clusters are thrown out. Cluster and sequence tables (TAS data structures) are filled with pointers back to relevant data in the pixel table.

The TPC hit finder, *tph*, takes the found clusters as input, and extracts the 2-dimensional padrow crossing position of tracks that created the cluster. In principle, this requires deconvolution of multipeak clusters, which is currently not implemented. Therefore, all work has been done with low track density simulated events. The two-dimensional shape of a single-track cluster may be calculated, and depends on the drift length and the crossing angles of the track with respect to the pad direction and the time direction. Fig. 4 displays some zero-noise examples of cluster shapes. In principle, one should perform a two-dimensional fit to the clusters to extract centroid information. Currently, however, a mean and a width are calculated for each direction (time-direction and pad-direction). To extract some 2-dimensional information the "orientation" of the hit with respect to the pad-plane is also calculated. Indicated in Fig. 4 are cluster centroids and orientations calculated by the space-point extraction algorithm. The orientation information should prove useful to follow-your-nose tracking algorithms, because, on the basis of its orientation, a hit may be rejected as belonging to a track whose crossing angles are approximately known.

Results

Tests with the slow simulator show that nearly all generated ionization clusters from sparse events are found by the *tcl* software. Current tests have been performed with sparse events only, and mostly with unrealistic noise values, but already processing such data has helped identify problems. Shown in Fig. 5 is the spatial resolution in the global x-direction for events with realistic noise (800 e^- RMS). The global x- and y- directions span the pad planes, while the z-direction lies along the drift direction. The y-resolution is identical. Fig. 6 shows that the resolution along the z-direction is better, but there is a long tail to the distribution. This effect is presently not understood, and persists even when one uses a realistic pulse shape to fit the time-pulses, instead of using a weighted mean.

Summary

In summary, the framework for cluster-finding and hit-reconstruction routines for the TPC are in place. The cluster finder reliably finds "islands" in the two-dimensional pad row – time bucket space, and may be considered near final form. Meanwhile, the hit finder currently employs a crude algorithm that takes a weighted mean in the pad and time directions, and transforms the mean to global TPC coordinates. Further work is needed for this routine in order to understand the z- (time) resolution, to perform truly two-dimensional cluster fitting, and to implement deconvolution of multi-peak clusters.

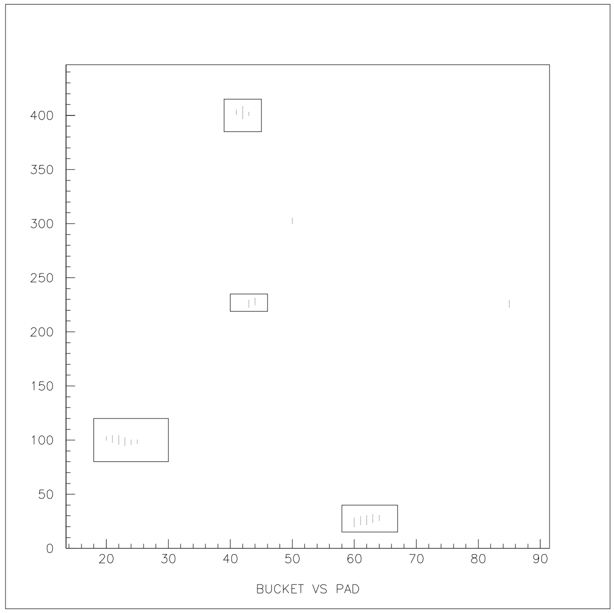

Figure 3: Sequences in time bucket versus pad number space for sparse event on inner sector pad row.

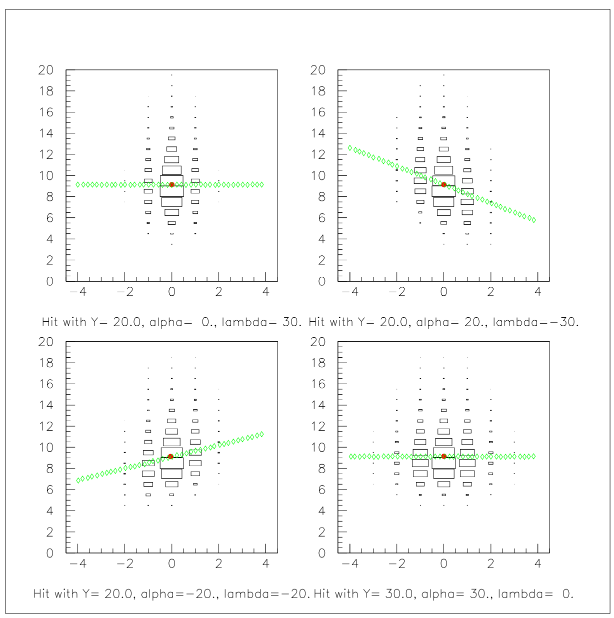

Figure 4: Examples of cluster shapes with zero noise; time versus pad number.

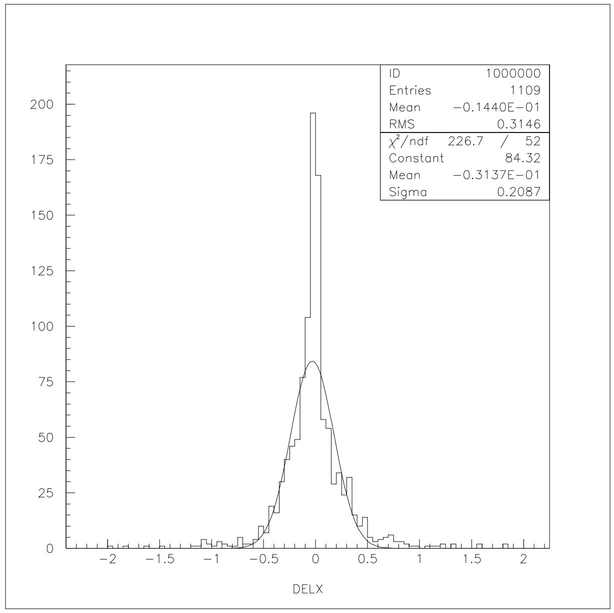

Figure 5: Spatial resolution in global x-direction (cm) with noise.

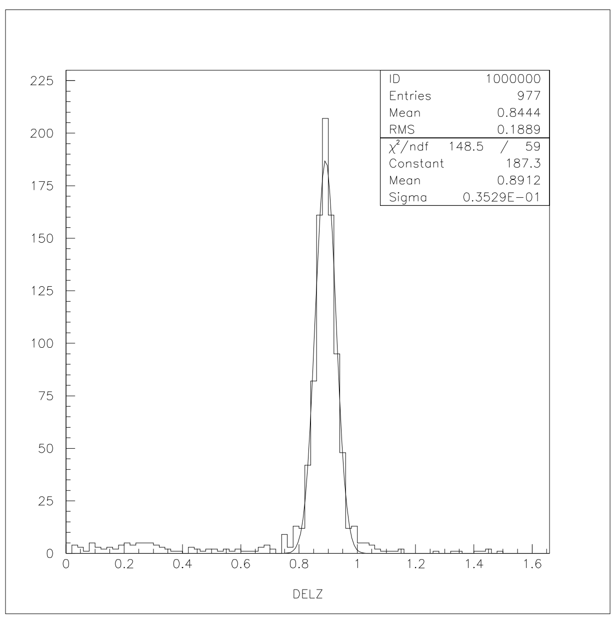

Figure 6: Spatial resolution in drift (z) direction (cm) with noise.

2.3 Time of Flight Performance

Contributed by: Pablo Yepes

The Time of Flight (TOF) system in STAR provides particle identification (PID) capability which substantially extends the particle species separation that is achievable with the baseline detector. In this note the algorithms used in the simulations and reconstruction programs along with their performance are briefly reported.

Time of Flight Algorithms

The full STAR Monte Carlo program, based on the GEANT package, is used to simulate the detector response to particles produced in heavy ion collisions. The TOF time resolution is determined according to the results obtained in a test beam [6] using the expression: $\sigma_t = \alpha\sqrt{z_t}$, where z_t stands for the distance from the particle impact to the phototube cathode and $\alpha = 30$ ps$/cm^{1/2}$.

The information resulting from the Monte Carlo simulation is run through the STAR analysis shell (TAS). The PID is done by the *cpi* module, the algorithm can be summarized in the following steps:

1. Extrapolation of tracks out to TOF barrel and back to the vertex. Tracks have to fulfill the following conditions to be further considered in the analysis:
   (a) Extrapolate to the TOF.
   (b) Originate at the main vertex.
   (c) Hit a TOF counter that has fired.
2. The length of the track from the interaction point to the TOF, L, is calculated.
3. The time provided by the TDC is corrected to take into account the light trajectory inside the scintillator. The corrected time, t_c, is obtained from the raw time, t_r, through the expression: $t_c = t_r - z_t v_s$ where a value v_s=75 ps/cm is obtained from the beam tests.
4. The particle velocity is obtained using the equation:

   $$1/\beta = ct_c/L = c(t_r - z_t v_s)/L \ .$$

As can be noted, the ability to separate the different particle species depends on the accuracy with which the various quantities in this equation can be determined. In the next section, resolution of some relevant quantities are discussed.

Resolutions

Fig. 7 shows the distance between the reconstructed impact using the TPC tracks and the real particle hit obtained from Monte Carlo information. The first plot presents the distance in rϕ, ϕ being the azimuthal angle. The second distribution represents the distance along the z-axis parallel to the beam. Both

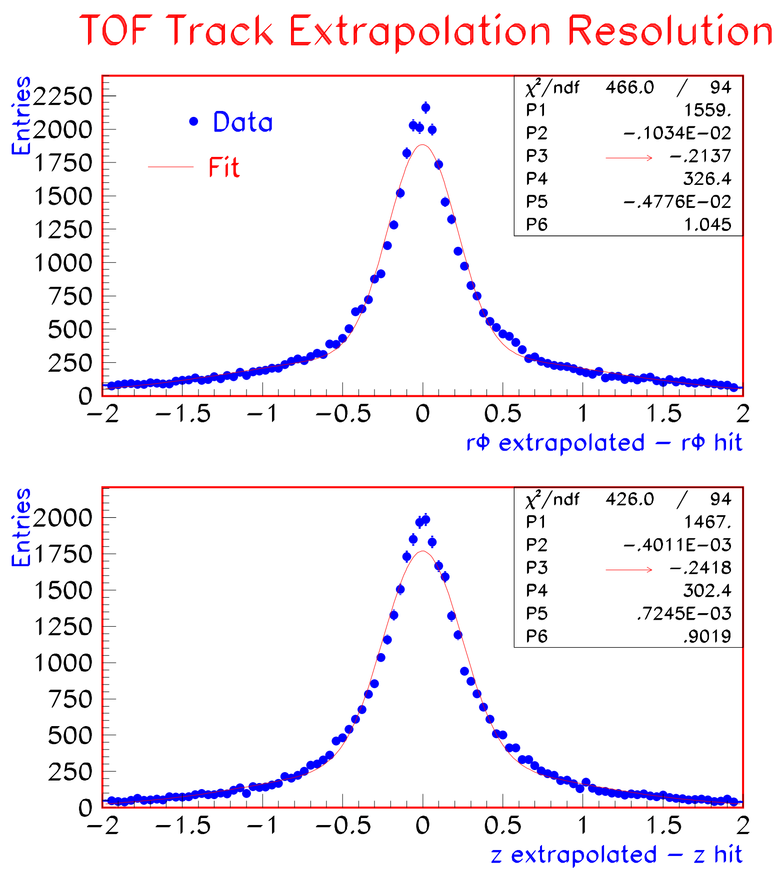

Figure 7: The distance between the reconstructed impact and the real hit from Monte Carlo (a) in rϕ and (b) along the beam axis (z). Reconstructed impacts are obtained from extrapolation of TPC tracks. The line is a double gaussian fit to the distribution.

distributions are fitted with a double gaussian. The width of the narrower gaussian, taken as the resolution, is 0.21(0.24) cm for the rϕ(z) distribution.

Fig. 8 depicts the difference between the corrected reconstructed time, t_r, and

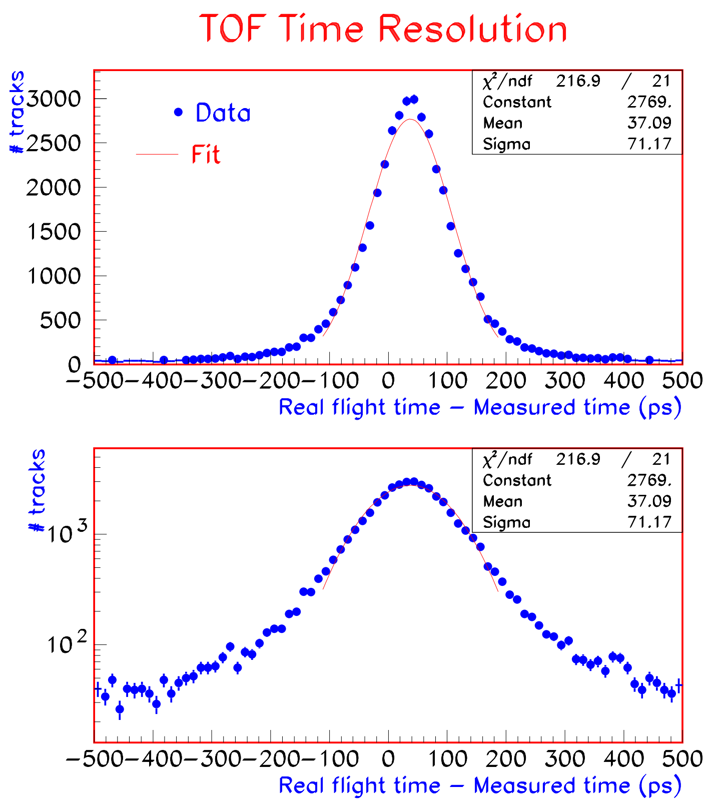

Figure 8: The difference between the corrected reconstructed time and the real impact time obtained from Monte Carlo. The upper (lower) plot is a linear (log) scale. The line represents a gaussian fit.

the real time obtained from the Monte Carlo. The distribution is fitted with a gaussian. The width of the distribution is 71 ps.

Fig. 9 shows the difference between the reconstructed track length and the real track length from the Monte Carlo. The reconstruction algorithm assumes that all tracks come from the main vertex. The Monte Carlo length is taken from the track origin to the back plane of the TOF. Reconstructed length is taken from (0,0) in the plane perpendicular to the beam to the front plane of the TOF. This difference in the calculation of the reconstructed and simulated lengths explains why the distribution is not centered at zero. The resolution in the track length determination is 0.8 cm.

Particle Identification Capabilities

In the base line detector, PID is done using the fact that pions, kaons, and protons are not minimum ionizing in the energy range of the STAR acceptance and

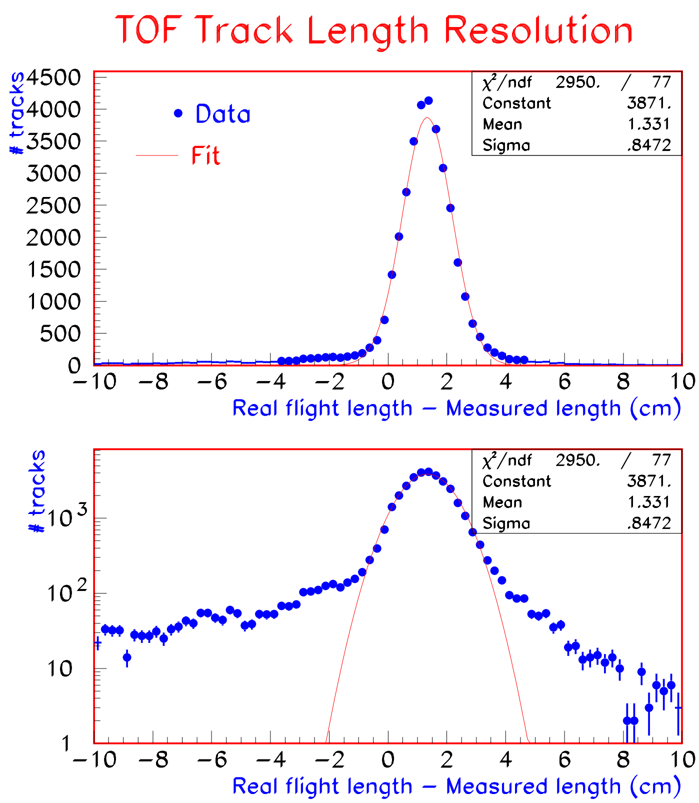

Figure 9: The difference between the reconstructed length and the real track length obtained from Monte Carlo. The upper (lower) plot is a linear (log) scale. The line represents a gaussian fit.

thus exhibit different energy loss while traversing the SVT and the TPC. Fig. 10a shows the expected energy loss curves measured in the TPC in the momentum

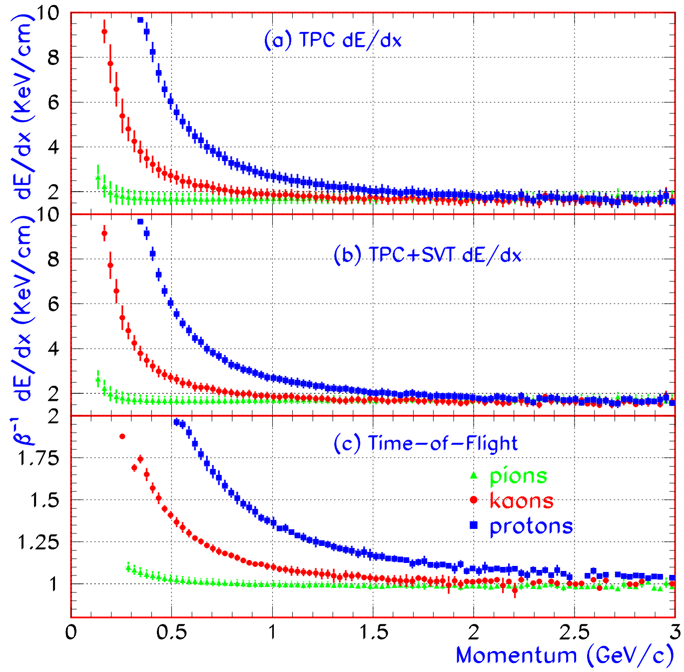

Figure 10: Particle identification distributions for (a) dE/dx in the TPC alone, (b) dE/dx for TPC+SVT (see text for explanation), and (c) time-of-flight information. Plotted is the mean value of the measured quantity as a function of particle momentum. The error bars are one standard deviation of the distribution at the measured momentum.

range 0-3 GeV/c for pions, kaons and protons. The plots in Fig. 10a were obtained by running the STAR GEANT Monte-Carlo program to simulate detector response and energy loss processes in the detector. From this figure, one can see that it is possible to distinguish kaons and pions below 600 MeV/c knowing their momentum and energy loss.

To perform PID from the TPC energy loss curves, functions of the Bethe-Bloch form (i.e., β^{-2}) were fitted to these curves. From these functions one can calculate the difference between the average expectation for a pion, kaon, proton, etc. at that momentum, and the measured energy loss for a given particle. The probability that a given particle belongs to each of the three species can be derived knowing the width of the dE/dx distribution and the difference in energy loss. At low momenta, where the pion/kaon separation is large, it is sufficient to take the highest probability hypothesis as the PID. Above 350 MeV/c, however, the pion and kaon dE/dx distributions overlap and the contamination (i.e. pions misidentified as kaons and vice-versa) becomes large. One can improve efficiency while maintaining low contamination by allowing more kaons from the high dE/dx side of the distribution to be tagged as kaons and more pions from the low dE/dx side of the pion dE/dx distribution to be tagged as pions, while cutting very hard on dE/dx values which lie in the overlap region. Using a method similar to this, one can get the efficiency and contamination distributions shown in Fig. 11a and b, plotted as a function of p_T. From these figures we see that proton identification

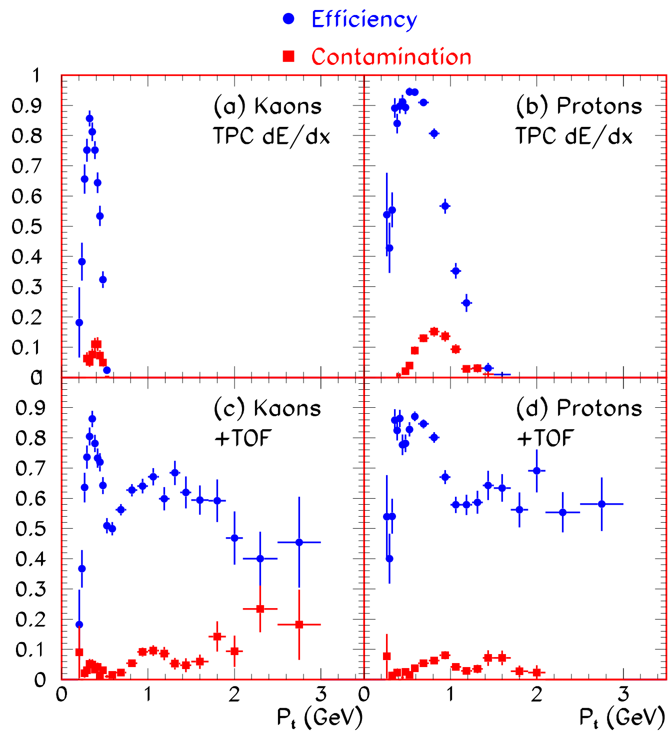

Figure 11: Efficiency and contamination levels for particle identification plotted as a function of transverse momentum for kaons and protons. Efficiency is defined as the total number of correctly tagged particles divided by the total generated in the Monte-Carlo. Contamination is defined as the number of incorrectly tagged particles divided by the number of correctly tagged particles. Parts (a) and (b) are for TPC dE/dx particle identification only, and (c) and (d) are obtained with combined dE/dx and time-of-flight information.

from energy loss in the TPC is feasible to $p_T \approx$1.2 GeV/c, while kaon identification is only feasible to $\approx$600 MeV/c.

Particles also experience energy loss while traversing the Silicon Vertex Tracker (SVT). The measured energy loss in this detector can be used as in the TPC for PID. Fig. 10b shows the TPC dE/dx distributions with the resolution improved by

	Contamination <10%	Contamination <50%
dE/dx π/K	<0.35	<0.65
+TOF π/K	<1.5	<2.0
dE/dx K/p	<0.7	<1.5
+TOF K/p	<2.5	<3.0

Table I: Upper limit in the momentum range where particle separation is possible with TPC dE/dx and TOF.

$\sqrt{2}$, which would be the effect on the PID capability if the SVT dE/dx information were equal to that of the TPC. This is an optimistic view given the fact that the momentum and dE/dx resolution in the SVT are likely to be worse than in the TPC. From the curves in Fig. 10b, we see that the separation for the different species is only slightly better, improving the upper limit for separation by ≈100 MeV/c.

The addition of a TOF system to the STAR detector will enhance PID capability in the momentum range covered by dE/dx in the TPC, and extend the useful range to 3 GeV/c. Fig. 10c shows $1/\beta$ versus momentum for pions, kaons, and protons. The excellent separation of the different particle species allows one to identify these particles at much higher momenta than using dE/dx alone.

PID from the TOF information is done in a similar way to that described above for the dE/dx information. Fig. 11c and d show efficiency and contamination for a combined TOF and dE/dx PID as a function of p_T.

Table I presents the momentum ranges where the different species can be separated with TPC dE/dx and with TOF. Two levels of maximum allowed contamination are considered.

2.4 External TPC Performance and Simulations

Contributed by: Jim Draper

The two external TPCs (XTPC) for STAR are intended to provide tracking and charge determination for forward and backward going charged particles with $|\eta|>2$. The objectives of the simulation study reported here are to: (a) show why the two XTPCs must be placed as close as possible to the magnet pole tips, (b) describe simulations and results for charge, momentum and η resolution of the XTPC, (c) outline the tracker algorithm, rejection of secondaries, and tracking efficiency, (d) show quantitatively how multiple Coulomb scattering (MCS) from the beam pipe and the SVT limits the performance of XTPC, and (e) illustrate the photon multiplicity detector (PMD) application.

Fig. 12-F1 shows the geometry with the first part of the XTPC at z= 385 cm. Calculations will be discussed for polar scattering angles θ = 2, 8 and 14 degrees; such lines are indicated in Fig. 12-F1 with their corresponding values of pseudorapidity, η, where $\eta = -\ln(\tan(\theta/2))$.

Fig. 12-F2 shows a model magnetic field that elucidates the placement of XTPC. It is like the STAR field, except that here the pole tip does not have a hole inside $\eta = 2.0$. The cylindrical Gaussian surface must have zero net magnetic flux through it, which gives a relation between the uniform, purely axial field, B_z, before the iron, and the radial field, B_r, inside the iron end. With this, the line integral of B_r (through the iron) along a constant radius increases linearly with radius.

In Ref. [7] this model field was used to calculate particle trajectories through the XTPC analytically in the limit that the thickness of the iron end goes to zero, while maintaining unaltered the line integral of the radial field. The line integral at r= 50 cm is called INT50. These trajectories, for a particular value of INT50, match very well the trajectories found with the realistic field of Schleuter using Poisson.

In order to understand the results, the twist must be defined. All tracking is done in the x,y plane. Fig. 12-F3 shows the x,y projection of tracks for momenta 0.2, 0.5, 1.0 and 2.0 GeV/c, as found by GEANT (physics off) with the realistic field map mentioned above. Eight hits are shown for each track, one for each plane of XTPC. A straight line is drawn beside each track to clarify the smallness of the curvature of the track due to the fringe field from the hole in the STAR pole tip. The twist is defined as the angle between a line from the first-plane hit through the origin of the coordinate system in Fig. 12-F3 and the line of the track. If the track is perfectly radial, the twist is zero. The twist is the measure of momentum and charge in XTPC, so it is of fundamental importance.

Fig. 12-F4 shows the product of twist and momentum, p, vs INT50, if INT50 could somehow be separately controlled without changing B_z. In all figures, θ is indicated by + for 2, o for 8 and x for 14 degrees. A later figure will show that twist is inversely proportional to p for p$\geq$ 1 GeV/c, hence the product. The twist

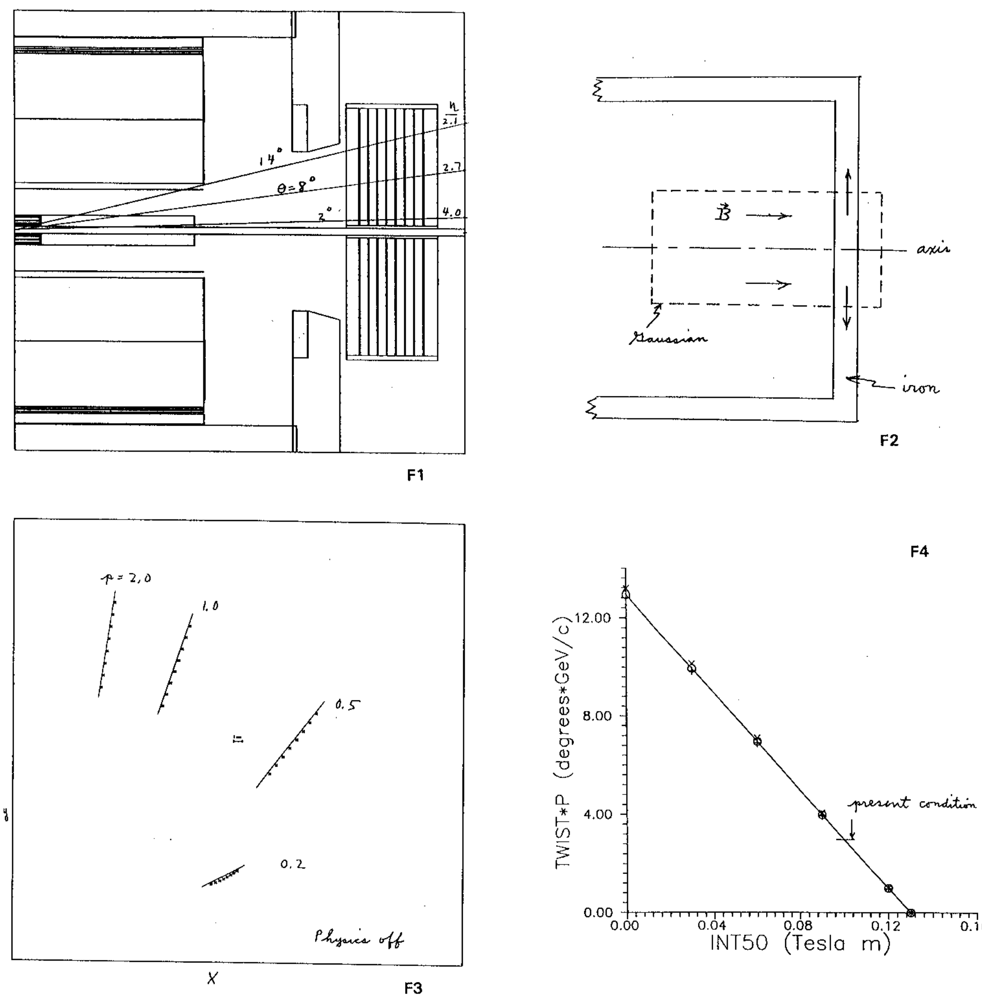

Figure 12: XTPC figures F1 - F4

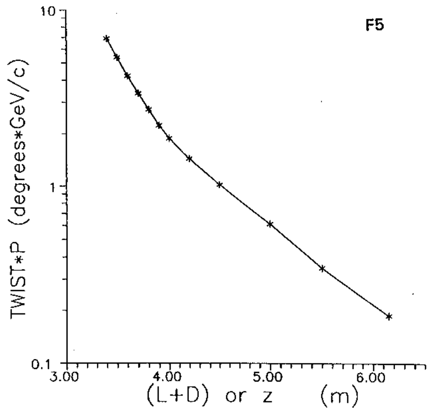

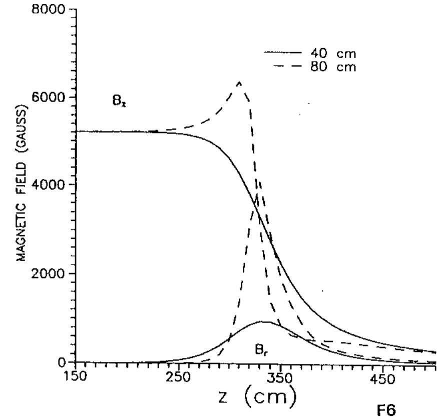

These two plots determine momentum and θ by iteration. Present one-step reconstruction is OK approximation for p> 1 GeV/c; now know simple remedy (STAR Note 187). z= 385 cm, empirical INT50.

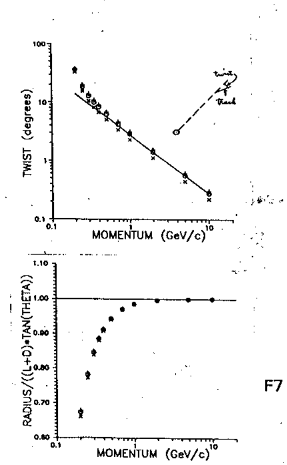

To reject secondaries

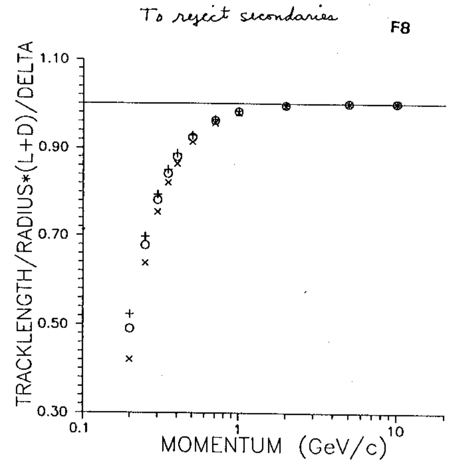

To reject secondaries

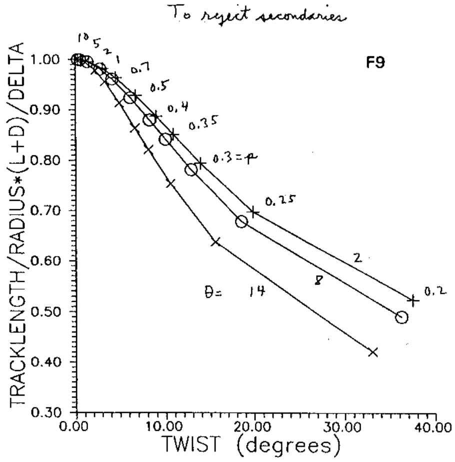

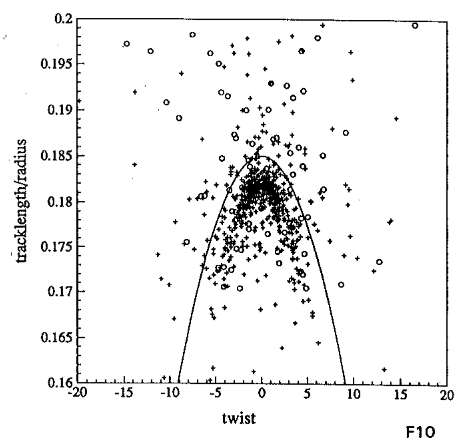

Figure 13: XTPC figures F5 - F10

TRACKER ALGORITHM

(1) Figure gives hit separation (track length) of 1-cm search circles vs hit radius. First pass is search angle = 0 (i.e. line of sight; OK for p > ~ 1.5 GeV/c).
(2) Remove 8-hit data after first pass.
(3) Zigzag as we increase search angle; Figure changes hit_separation/radius vs search angle (twist).
(4) Could use changing curving (small p) search shape as search angle increases.

F11

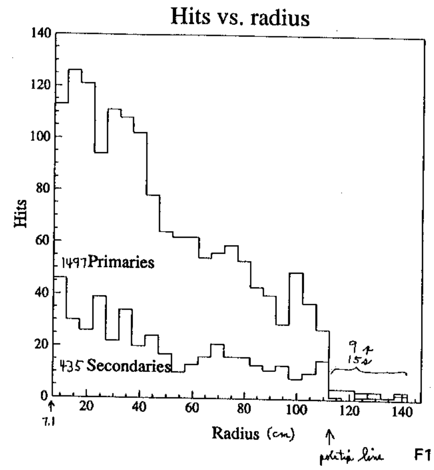

F12

TRACKER EFFICIENCY; SECONDARY REJECTION

Some rejection is already in tracker; can further cut below upper parabola. (PAW would not accept an additional lower parabola function).

For P_g> 1 GeV/c; central AuAu Lund event; hit radii < where track leaves XTPC; require 8 hits:

1180/1248 = 95% of primaries tracked; no upper parabola cut.

1066/1248 = 85% of primaries survive with upper parabola cut. Difference is large-angle scattered, so OK.

35/435 = 8% of secondaries survive upper parabola cut.

(147/435 = 34% of secondaries survive without upper parabola cut).

Further tuning and speeding of tracker is under way.

F13

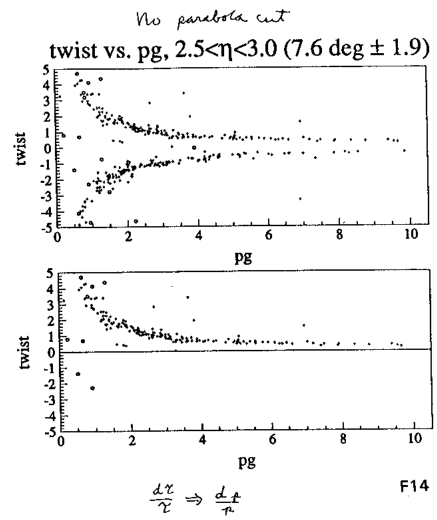

F14

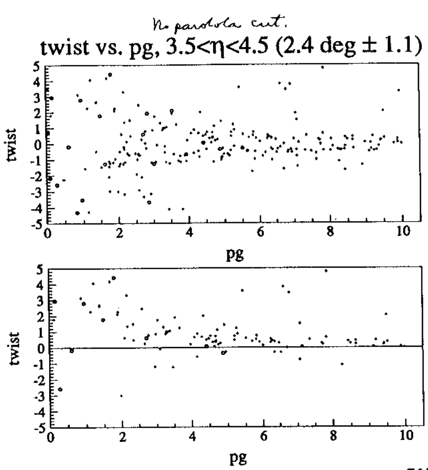

F15

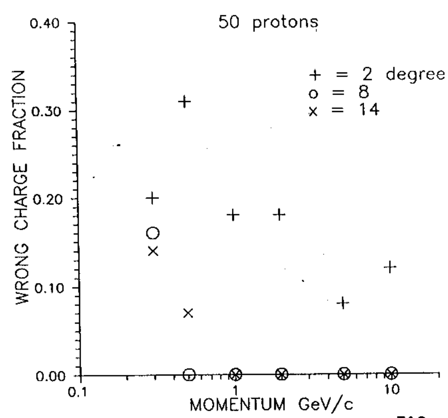

F16

Figure 14: XTPC figures F11 - F16

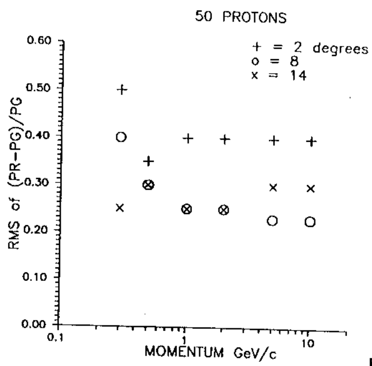

F17

central AuAu, Sund

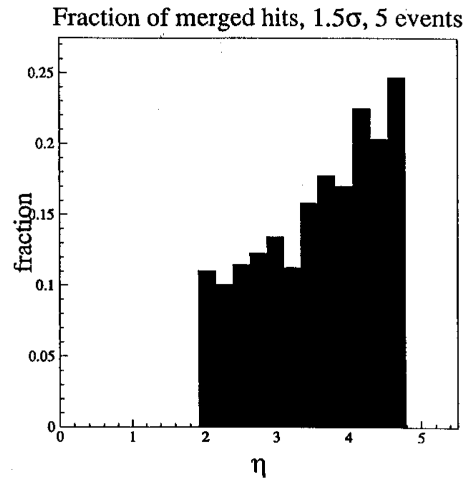

F18

EFFECT OF MAGNETIC FIELD ON ELECTRON DRIFT

Langevin equation.
$\omega\tau = \mu B$, corrected as in ALEPH.
Biagi's μ for real electric field/P10.
Realistic magnetic field.

For hit at r= 10, collect at r=125 cm:

z cm	spiral angle	z drift
380	9.3 degrees	0.71 cm
390	8.6	0.58

F19

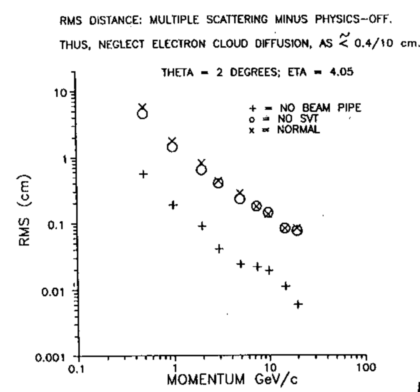

F20

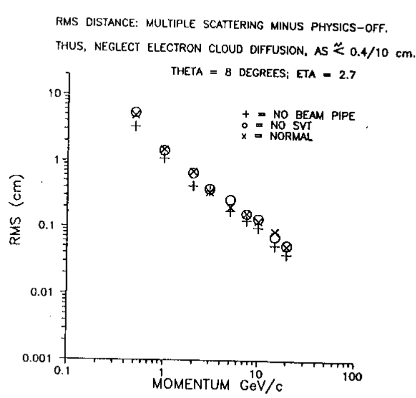

F21

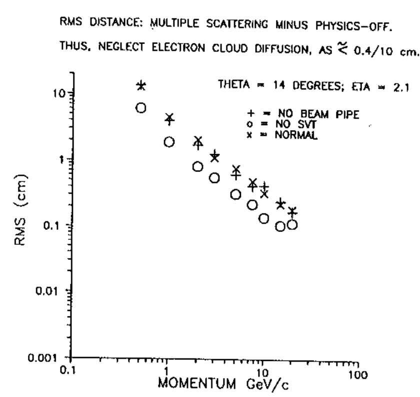

F22

Figure 15: XTPC figures F17 - F22

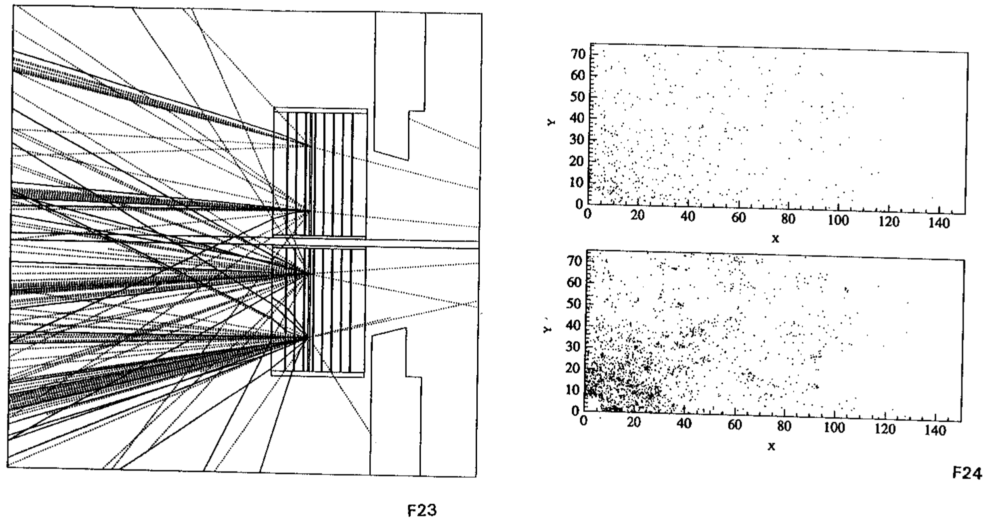

Figure 16: XTPC figures F23 - F24

vanishes at INT50= 0.13, which is the value of INT50 from Gauss's law in Fig. 12-F2. This vanishing is independent [7] of momentum, θ, B_z or the length of B_z. For INT50= 0.13, the twist produced by B_z is undone by deflection in B_r. Thus, there would be no twist if the STAR pole tip did not have its hole. However, the hole allows B_r to spread beyond the pole tip, so placing XTPC close to the pole tip means that INT50 is reduced, and twist is regained. If XTPC were placed just inside the STAR solenoid, at INT50= 0, then the twist would be as shown at the left edge of Fig. 12-F4. The empirical value of INT50 that gives model trajectories almost identical to GEANT is marked in Fig. 12-F4.

The model is useful in studying a variety of geometries and conditions. Fig. 13-F5 shows the model results, spot checked with GEANT, for twist$\times$p vs the z of the first plane of XTPC. Presently z is 3.85 m. One sees how the twist increases rapidly as XTPC is moved closer to the pole tip.

Fig. 13-F6 shows B_r and B_z for r = 40 and 80 cm in the realistic field map. Numerical integration of B_r from z=0 to any fixed z, e.g. 3.85 m, gives near linearity with r. The small nonlinearity is evaluated and used in [7], as well as in all relevant figures here.

Fig. 13-F7 shows the twist vs p and the radius (divided by tanθ) of the first-plane hit vs p from the model, again matching closely the results from GEANT with the field map of Fig. 13-F6. The line is 2.78/p. The upper panel shows that the twist is closely related to p, but requires some knowledge of θ. Conversely, the lower panel shows that the first-plane hit radius is a good measure of θ, but requires some knowledge of p. By iterating between the two panels of Fig. 13-

F7, one can get an extremely accurate evaluation [7] of p and θ for any track, in absence of MCS. The present tracker algorithm does a one-step approximation to this iteration which suffices for $p \geq 1$ GeV/c. However, the iteration will be incorporated, and requires little extra time since excellent accuracy is obtained with only two iterations. Fig. 13-F7 again illustrates the definition of twist.

So only twist and first-hit radius are sufficient to determine uniquely p and θ for a primary track. To exhaust the significant properties of the track, one must include track length, or distance between successive hits in Fig. 12-F3. Fig. 13-F8 shows the ratio of track length to radius vs p. The factor (L+D)/DELTA is z/(XTPC thickness)= 385/70= 5.5. The content of Fig. 13-F8 is used in the tracking algorithm to reject some secondaries, as seen below.

Fig. 13-F9 shows the ordinate of Fig. 13-F8 vs twist (i.e., all the measurables, unless the track is significantly curved), and illustrates how cuts can be made to reject secondaries. Since $\theta = 2$ to 14 degrees approximately spans the range of possible trajectories into XTPC, each primary must lie approximately between the two outer curves of Fig. 13-F9. For larger p, these curves approximate parabolas. Thus, Fig. 13-F10, shows a parabolic cut to help distinguish primaries from secondaries. This is a AuAu central event run through GEANT (physics on), tracked and analyzed with our programs. GEANT primaries are denoted by + and secondaries by o. All tracks above the parabola were rejected. A lower-bound parabola peaking at about 0.175 would also have been useful, but could not be activated due to techinal details. In addition to this cut, once p and θ are evaluated, such a primary is a particular point [7] in Fig. 13-F9, and secondary rejection can be further refined.

Fig. 14-F11 summarizes the tracker algorithm used after GEANT. Again, all quantities are in the x,y plane, perpendicular to the RHIC beam. The search angle (SA) is measured with respect to the line of sight (i.e., first-plane hit to x,y=0). The first pass is with SA=0 and with the eight search circles (1 cm radius) spaced at intervals of 1/7 of the track length (shown in the right hand region of Fig. 13-F8), starting from a first-plane hit. An acceptable track was required to have eight such hits. The track is the least-squares fit to those eight hits. Then those eight hits are removed from the data pool. After the first pass through all the first-plane hits, the second pass is with SA=arctan(1 cm/track length), with track length taken from Fig. 13-F8. If no track is found, the same SA with the opposite sign is tried. This process is continued, incrementing SA, until a track is found or some arbitrary limit like SA= 45 degrees. Since SA is analogous to twist, closely related to momentum, then Fig. 13-F8 is used to relate track length to SA. Thus, some of the secondaries and the heavily scattered primaries (i.e., information content already lost) are rejected in this search process. This will be further refined, later.

Fig. 14-F12 shows the distribution, and relative numbers, of primaries and secondaries vs radius (x,y plane) for a central AuAu event.

Fig. 14-F13 describes the tracking efficiency. In summary, 95% of primaries are tracked, with some heavily scattered ones having been properly rejected by the

hit-spacing requirement, since they no longer contain correct information. Some of these are further rejected by the parabola cut, leaving 85% of all primaries tracked as not being too heavily scattered. With the parabola cut, only 8% of the secondaries sneak through.

Fig. 14-F14 shows measured twist in AuAu vs GEANT momentum, for a band of θs near 7.6° (recall the θ dependence in the upper panel of Fig. 13-F7). The lower panel of Fig. 14-F14 is for one sign of GEANT charge, and shows that here the sign of charge (i.e., sign of twist) is correct for all primaries (secondaries are open circles). The fractional vertical width of the band is approximately the fractional momentum resolution, since Fig. 13-F7 shows twist nearly proportion to 1/p. This observation is to elucidate, but is not the way that momentum resolution, below, was evaluated.

Fig. 14-F15 is like Fig. 14-F14, but for θ near 2.4°, where Fig. 12-F1 shows that the beam pipe will produce considerable MCS. However, only a few twist signs (charge) are wrong.

Fig. 14-F16 shows the charge resolution of XTPC for GEANT plus MCS with the three θs, and 50 protons at each θ and each momentum. For $p \geq 1$ GeV/c and $\theta = 8°$ or 14°, the sign of charge (sign of twist) is correctly measured for all 50. For $\theta = 2°$, where beam-pipe MCS is a problem, $\sim 15\%$ are measured as the wrong charge.

Fig. 15-F17 shows the momentum resolution of XTPC, again for GEANT with 50 protons each at three θs and six momenta. Since some primaries are heavily scattered and the distribution is non-Gaussian, the RMS means the value that contains 2/3 of the protons. For $p \geq 1$ GeV/c, $\theta = 8°$ or 14°, the momentum resolution averages about 26% in Fig. 15-F17, with the worst case again being at $\theta = 2°$, with much MCS from the beam pipe.

Fig. 15-F18 shows the fraction of merged hits vs pseudorapidity. We have calculated in detail the RMS radius, σ, of the electron cloud when collected, using Biagi's diffusion parameters as a function of the inverse-radius electric field in the cylindrical-drift XTPC. The merging criterion was chosen as two first-plane hits being closer than 1.5σ.

With XTPC being placed close to the STAR pole tip in order to be upstream of some of the radial field, this means that the upstream part of XTPC has significant magnetic field, see Fig. 13-F6. The resulting effect on the electron drift in XTPC, Fig. 15-F19, was evaluated by means of the Langevin equation, which requires the field vectors E and B, and the quantity $\omega\tau$ which approximately equals μB (electron mobility μ). The Langevin equation was integrated, using the 1/r electric field and Biagi's values of μ, and the results are in Fig. 15-F19. The measured difference between $\omega\tau$ and μB in the ALEPH report was incorporated. The front and back of the first of eight planes in XTPC are at z= 380 and 390 cm, shown. The spiral angles for these are small and do not differ much, as is true of the drift along z. Thus, the effect is tolerable.

Figs. 15-F20 - 15-F22 show quantitatively the effect of MCS from the SVT and the beam pipe. Plotted is the RMS distance between a first-plane hit with no MCS (GEANT with physics off) and a first plane hit for the same particle with MCS on in GEANT. Again 50 protons were used for each point. The three symbols represent NORMAL (i.e., all of GEANT's STAR hardware present), and then NORMAL minus the beam pipe, or NORMAL minus the SVT. At $\theta = 2°$, Fig. 15-F20, the RMS distance is an order of magnitude smaller when the beam pipe is taken out. We are working on ways to decrease the substantial degradation in performance caused by the beam pipe. Fig. 15-F21 shows approximately equal RMS distances for all three conditions. Fig. 15-F22 ($\theta = 14°$) shows that MCS effects are about halved for $\theta = 14°$ when the SVT is removed. The most current SVT geometry information was not included in these simulations. Summarizing, the RMS distances are roughly the same for the following six plots: (a) all three cases with $\theta = 8°$; (b) $\theta = 14°$ without the SVT; and (c) $\theta = 2°$ with beam pipe present. Since the RMS distance uncertainty falls with p faster than the twist, the momentum resolution shown in Fig. 15-F17 tends to be flat at higher momentum.

Figs. 15-F20 - 15-F22 also enable determination of the uncertainty in measurements of η. For XTPC, this uncertainty is $\Delta\eta = \Delta\theta/\theta$. With $\Delta\theta$=RMS/385, the largest $\Delta\eta$ are near $\eta = 4.1$, where $\Delta\eta = 0.104$, 0.059, 0.016 and 0.0089 for p= 1, 2, 5 and 10 GeV/c, respectively. Thus, η can be accurately measured by the XTPC. Detailed calculations of electron drift in the 1/r field, including pad response, show that the collected cloud size (RMS radius) vs starting (hit) radius has a maximum at intermediate starting radii. This maximum RMS radius is 0.3 cm radially and 0.4 cm azimuthally. We expect to locate their centroids to better than 10% of this. Since this ($\sim$0.04 cm) is much less than the first plane hit position uncertainties due to MCS in Figs. 15-F20 - 15-F22, reconstructed space point position uncertainties in the XTPC will have negligible impact on the measurement errors in η.

Fig. 16 gives an indication of the photon multiplicity detector (PMD) aspects of XTPC. Here a 3-radiation-length slab of lead oxide (nonconducting) is placed between planes #5 and 6 of the XTPC at one end of STAR. In Fig. 16-F23 four 1 GeV photons from the collision were incident on the Pb. The shower positrons and electrons are indicated by solid lines, photons by dotted. These 3 radiation lengths give high efficiency, but substantial multiple scattering of the electrons. Fig. 16-F24 shows the hits in the XTPC plane just before the Pb (upper part) and the plane just after the Pb (lower part) for a AuAu event (GEANT, physics on). The downstream plane shows perhaps two dozen showers in one quadrant. It also shows a substantially increased number of isolated hits. We have not yet studied how much background is in the upstream parts of XTPC, produced by the Pb.

Our quantitative understanding of the reduction of twist (hence momentum and charge-sign resolution) caused by the radial magnetic field now leads us to analyse the relocation of these forward TPCs just inside the solenoid, before the radial field. This is being vigorously investigated.

Major contributions from Lynn Wood in navigating GEANT and from Juan

Romero in doing most of the FORTRAN programming are gratefully acknowledged.

2.5 Global Tracking Performance

Contributed by: Ricardo Mastroleo and Lanny Ray

Introduction

Charged particles with $|\eta| \leq 1$ and with sufficient transverse momentum ($p_T \geq$ 150 MeV/c) will produce hits in both the SVT and TPC, thus permitting improved determination of the particle's momenutm due to the extended track length and improved location of the particle's production vertex due to the very precise position resolution ($\sim 20\mu$m) of the SVT. Tracks which span both the SVT and TPC are referred to as *global tracks*. Not all particles traverse both detectors, however. Low p_T particles will not reach the TPC but can be tracked in the SVT; particles with $1 \leq |\eta| \leq 2$ can be tracked in the end regions of the TPC but not in the SVT; secondary particles from decays and from production vertices will leave tracks in the TPC but not necessarily in the SVT.

In this performance simulation study the momentum resolution and vertex position determing capability for global tracks in STAR are evaluated. For the latter we calculate the minimum distance between the inward, extrapolated track (helix) and the actual, Monte Carlo (MC) GEANT production vertex of the particle for both primaries and secondaries.

Method of Analysis

In order for a track to be successfully identified in the SVT there must be at least one hit on each of its three layers. If the ratio of active area per SVT layer to total area per layer is denoted by f_{active} (assumed to be about 95% in these simulations), then at most f_{active}^3 of the total number of charged particles that traverse each layer of the SVT will be identified and tracked. Further SVT tracking efficiencies, TPC tracking efficiency, and SVT-TPC matching efficiency (~85%) further reduce the fraction of SVT-TPC charged particle tracks that are successfully reconstructed. With the present reconstruction software and for typical FRITIOF Au+Au central collisions at 100 A·GeV/c about 1000 SVT-TPC matched tracks are successfully reconstructed, leaving about 1500 - 2000 remaining TPC tracks. Having identified these SVT-TPC global tracks a refit of the SVT and TPC space points is done, resulting in significantly improved momentum resolution and vertex position information for this important subset of tracks.

For the present analysis the following cases are considered: **Case 1** – all SVT-TPC matched and refitted tracks plus all remaining, unmatched TPC tracks, **Case 2** – SVT-TPC matched and refitted tracks only, and **Case 3** – TPC tracks only where the SVT was physically removed in the GEANT simulations. The global track refitting and evaluation were done using the analysis software package, *egr*. All tracks considered in Cases 1-3 are stored in TAS table, GLOBTRK, and for brevity will be referred to as global tracks.

The global track evaluator determined the following for each global track: (1) was there an SVT segment and if so was it valid (*i.e.* all assigned space points were from the same MC track), (2) was there a TPC segment and if so was it valid (*i.e.* at least 70% of the assigned space points were from the same MC track), (3) if both SVT and TPC segments exist and are valid was the matching done correctly, and (4) for "valid" global tracks (typically over 95% are "valid," meaning the SVT and/or TPC segments are valid and matching was correct) the differences between the reconstructed and MC total, longitudinal and transverse momenta and pseudorapidity were computed, as well as the minimum distance from the vertex. In this study the MC momentum at the vertex was used. Actual differences $(x_{rec} - x_{MC})$ and percent differences, $100\%(x_{rec} - x_{MC})/x_{MC}$, were computed. In the following we show results for the total momentum and distance from vertex for Cases 1, 2 and 3.

Results

Fig. 17 shows the distributions of total momentum percent differences for one Au+Au FRITIOF central collision for all SVT-TPC matched tracks (959) plus all remaining TPC tracks (1730) (Case 1). The six parts of the figure represent different total momentum ranges. From left to right and from top to bottom these ranges are (in GeV/c): all p_{tot}, $0 \leq p_{tot} \leq 0.25$, $0.25 \leq p_{tot} \leq 0.5$, $0.5 \leq p_{tot} \leq 0.75$, $0.75 \leq p_{tot} \leq 1.0$ and $p_{tot} \geq 1.0$. The typical momentum uncertainty (rms) is about 3% and it generally improves for the higher momentum ranges. The overall shift of each distribution to negative values is due to energy loss which increases in percent for the lower momentum ranges as expected.

Fig. 18 displays the same information as Fig. 17 for the same Au+Au event except that only the subset of valid, matched SVT-TPC tracks are considered (Case 2). In general the momentum resolution is about a factor of 2 better for this case. The benefit of the SVT with respect to improved momentum resolution, at least for the matched tracks, is evident in this figure.

Fig. 19 displays the same information as in the first two figures, except for Case 3 – valid TPC tracks with the SVT physically removed. The momentum resolution here is comparable to that in Fig. 17 for Case 1. Note that the average momentum loss is reduced in this case due to the removal of the SVT.

Figs. 20 - 22 display distributions of the minimum distance (in cm) between the inward, extrapolated track and the MC production vertex for each particle for Cases 1, 2 and 3, respectively. The six parts of each figure correspond to the same ranges in total momentum as in Figs. 17 - 19. The distributions for positive distance apply to primary particles; the negative values (-1 $\times$ min. distance) to secondary particles.

From Fig. 22, for TPC only, we find that the lowest momentum range is dominated by secondaries; primaries dominate at high momentum. In Fig. 21 it is observed that the SVT-TPC matched tracks are almost entirely primaries. For Case 1 (Fig. 20) secondaries are seen to dominate at low momentum, while primaries dominate at high momentum.

For Case 3 (TPC only, SVT removed, Fig. 22) the distance from vertex uncertainty is typically 0.5 - 1.0 cm for both primaries and secondaries. For Case 2

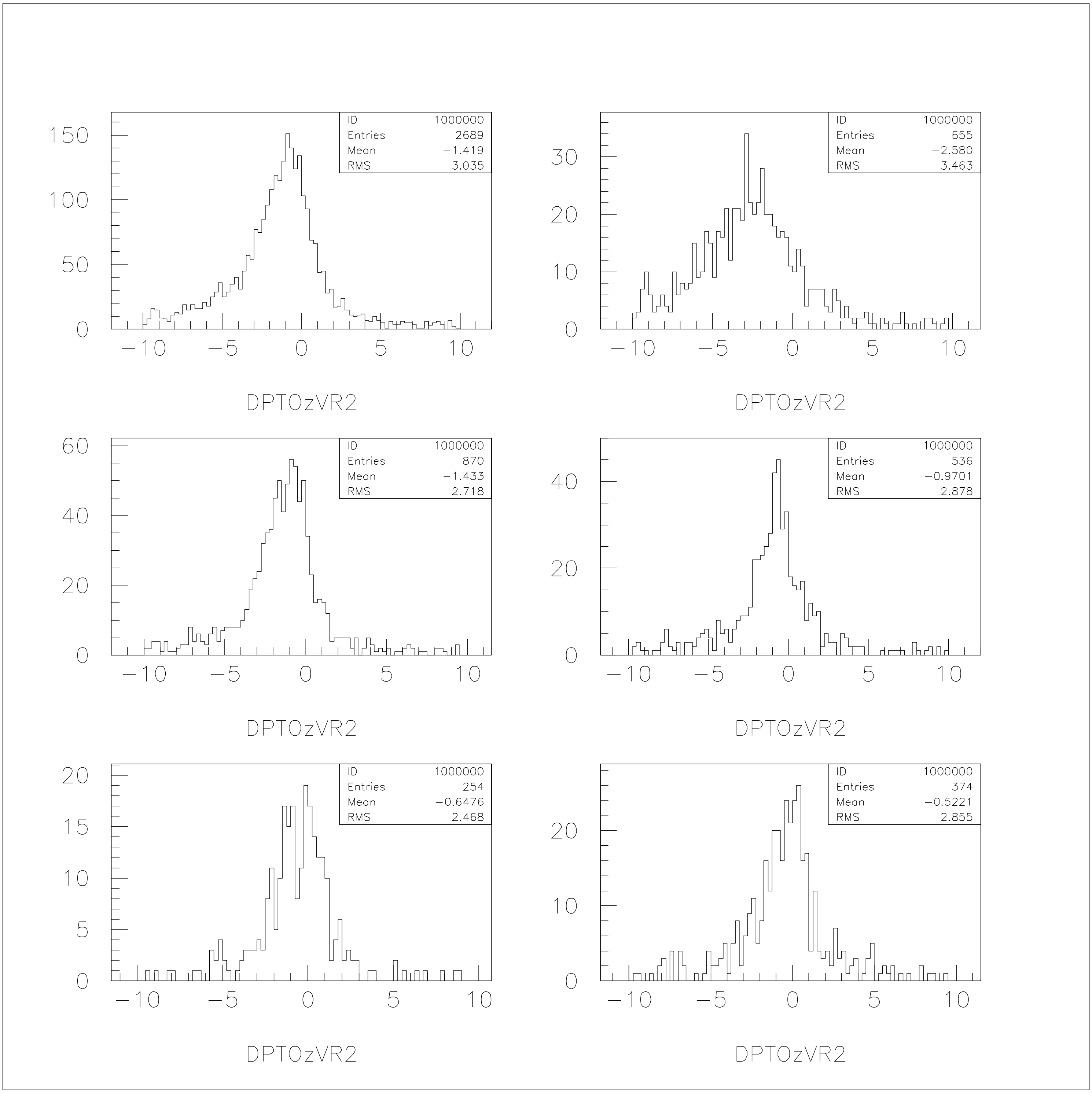

Figure 17: Total momentum resolution for Case 1: SVT-TPC matched tracks plus all remaining TPC tracks for different momentum ranges (see text).

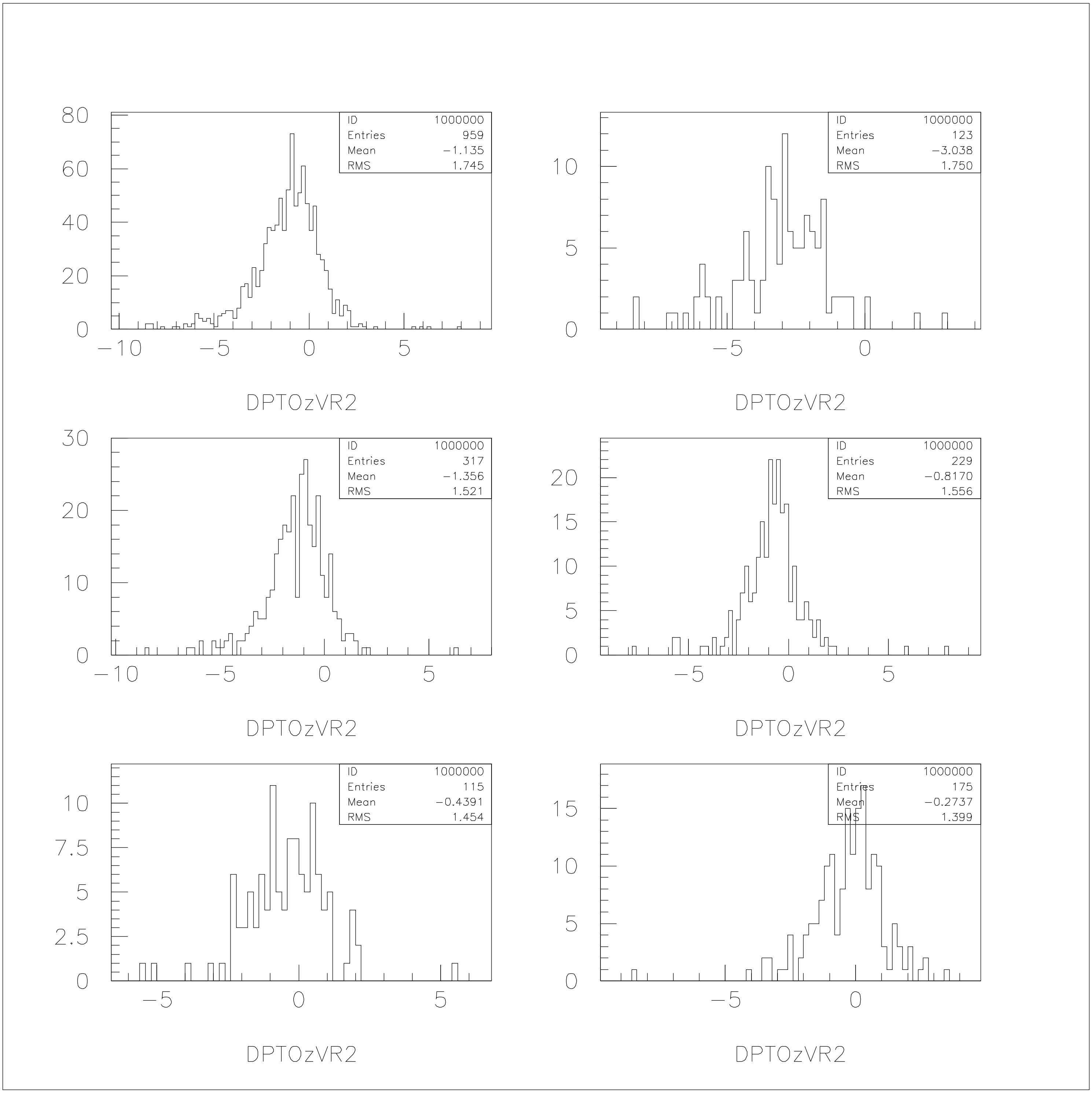

Figure 18: Total momentum resolution for Case 2: SVT-TPC matched tracks only for different momentum ranges (see text).

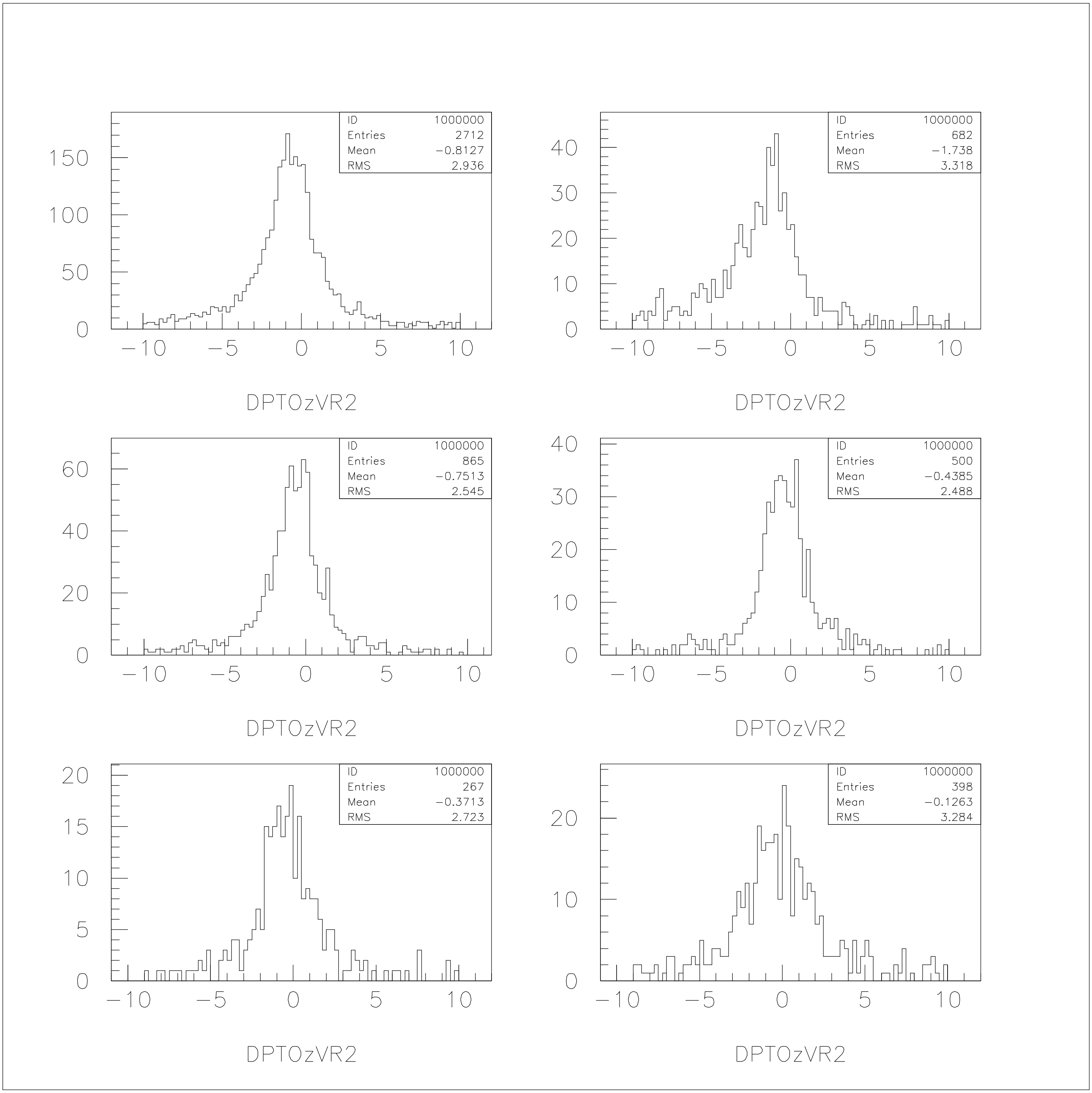

Figure 19: Total momentum resolution for Case 3: TPC tracks only, SVT physically removed, for different momentum ranges (see text).

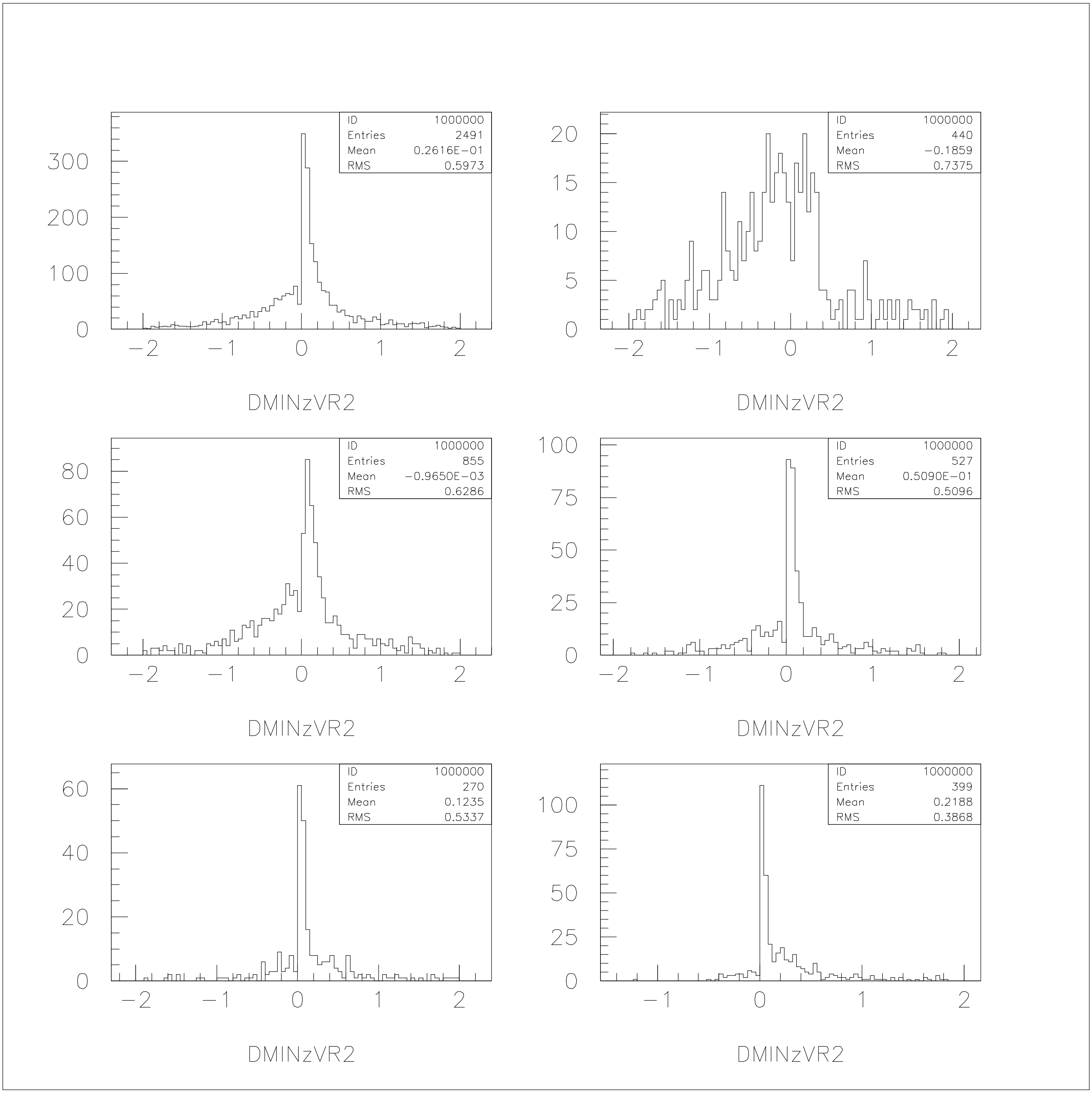

Figure 20: Distributions of minimum distance from vertex for Case 1: SVT-TPC matched tracks plus all remaining TPC tracks for different momentum ranges (see text). Positive (negative) values are for primaries (secondaries).

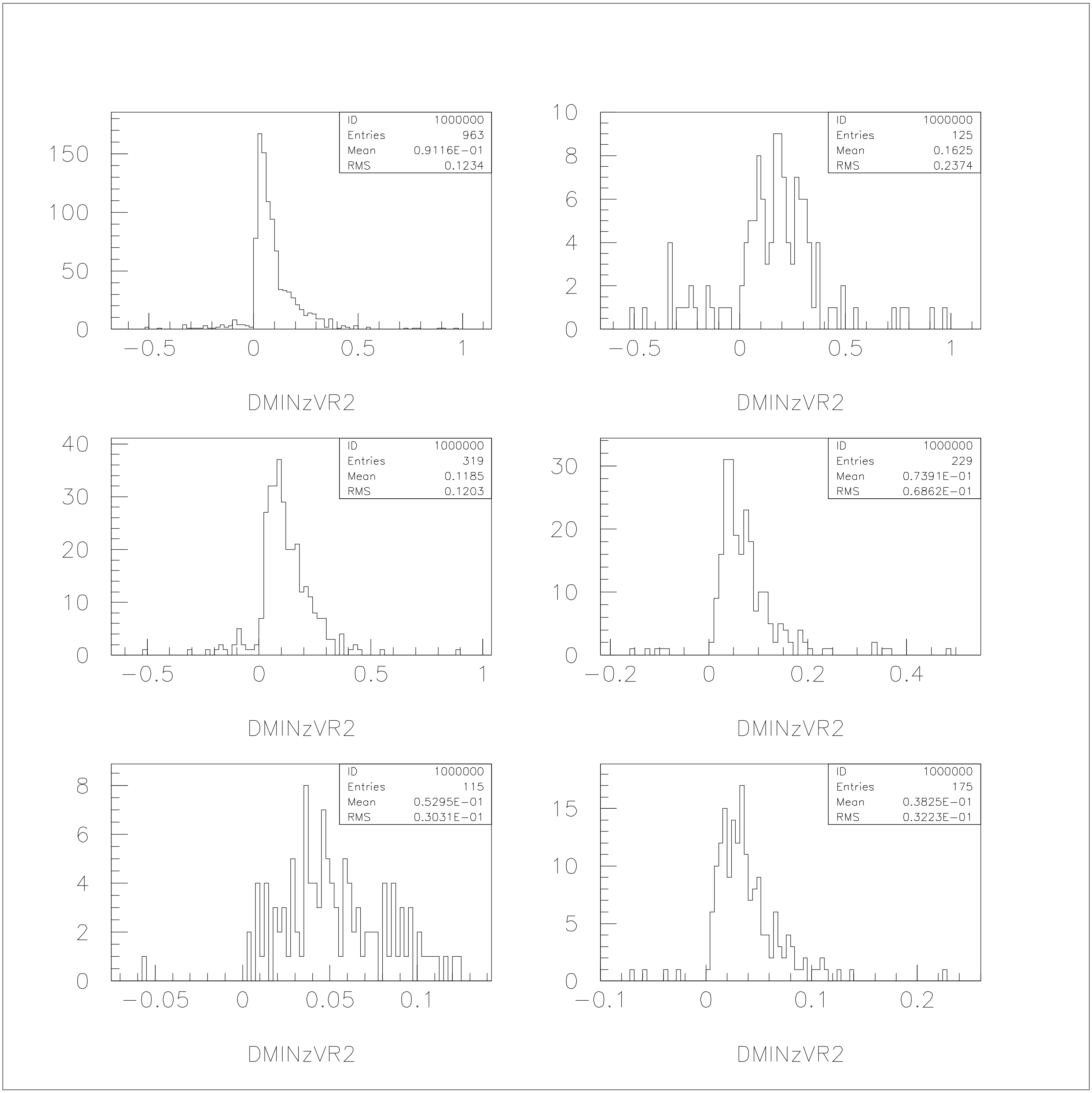

Figure 21: Distributions of minimum distance from vertex for Case 2: SVT-TPC matched tracks only for different momentum ranges (see text). Positive (negative) values are for primaries (secondaries).

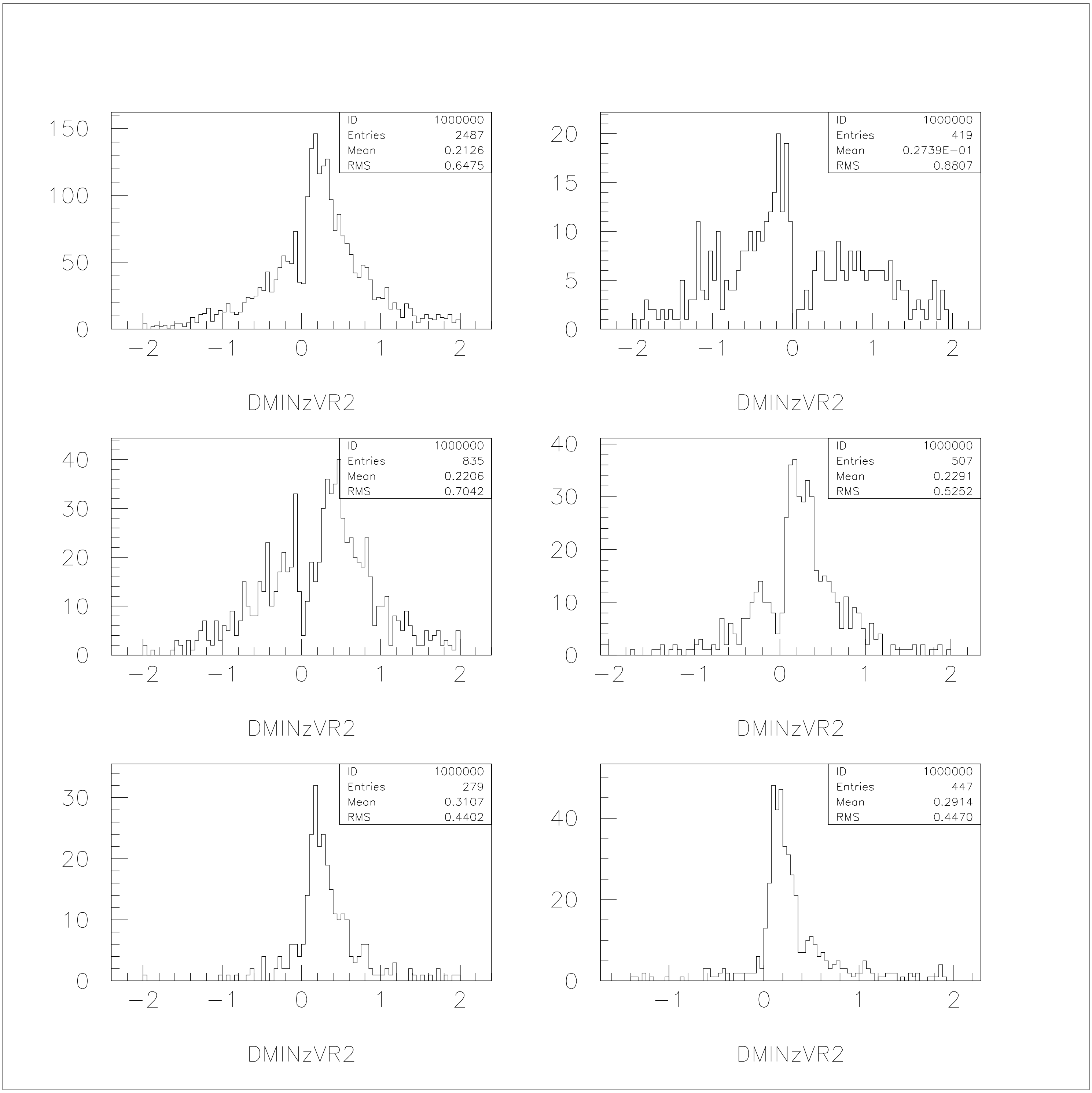

Figure 22: Distributions of minimum distance from vertex for Case 3: TPC tracks only, SVT physically removed, for different momentum ranges (see text). Positive (negative) values are for primaries (secondaries).

(SVT-TPC matches, Fig. 21) the distance from vertex uncertainty is about a factor of 5 - 10 smaller than that determined by the TPC alone. The distance from vertex uncertainty decreases dramatically from 0.2 cm to 0.03 cm as the momentum range increases. Adding the remaining TPC tracks (Case 1) to the SVT-TPC matched tracks gives the results shown in Fig. 20. The distance from vertex uncertainty for secondaries is comparable to the TPC only, Case 3, results, while for primaries the distance from vertex uncertainty for Case 1 is significantly better than that for Case 3. The point to make here is that the additional MCS produced by the SVT is more than compensated by the improved position determination for the tracks at the inner radii.

Summary and Conclusions

Total momentum resolution for the STAR baseline detector (TPC only) and for all tracks with SVT included is about 3% for momenta up to 1 GeV/c. For the subset of matched SVT-TPC tracks (about 1000 in central Au+Au) the total momentum resolution improves to about 1.5%. The projection of reconstructed tracks inward to the production vertex is uncertain by typically 0.5 - 1.0 cm for TPC only and is improved by almost an order-of-magnitude with the addition of the SVT for the subset of matched SVT-TPC tracks.

This research was supported in part by the U. S. Dept. of Energy, grant No. DE-FG03-94ER40845.

3 Analysis of Physics Capabilities

3.1 Event-by-Event Physics in STAR

Contributed by: Jeff Mitchell, Stathes Paganis and Lanny Ray

Introduction and Motivation

One of the unique features of STAR is its ability to determine global characteristics of the nucleus-nucleus collision in its final, hadronic state on an event-by-event basis. Of particular interest are the event-by-event determinations of charged particle multiplicities, temperature and mean transverse momentum ($\langle p_T \rangle$) for different particle species, particle production ratios, and pion source sizes. The need to characterize each event in this way is motivated by theoretical work which predicts the following: i) large event-to-event fluctuations in the above quantities in small kinematic intervals near the point of a phase transition from purely hadronic to a deconfined quark gluon plasma (QGP) [8] and ii) random, event-to-event reorientation in isospin space of the $q\bar{q}$ condensates in a QGP which lead to unusual $(\pi^+ + \pi^-)/\pi^0$ ratios [9]. In this analysis we investigate the capabilities of STAR with respect to several of these event-by-event measurements, specifically the pion temperature and $\langle p_T \rangle$, and the K/π ratio.

Method of Analysis

The analysis was based on Monte Carlo (MC) simulations using the following detector simulation and reconstruction analysis software chain: (1) the FRITIOF [10] event generator, (2) the STAR implementation of GEANT [11], (3) fast simulators for the SVT and TPC which approximate the detector ionization/electronic/DAQ response to the passage of charged particles as well as space point reconstruction (hit merging and finite spatial resolution effects were included), (4) SVT and TPC tracking, (5) SVT-TPC track-to-track matching, (6) global track refitting, (7) particle identification (PID) based on dE/dx in the SVT and TPC, and (8) numerous evaluation modules which compare the reconstructed event with the original MC event. Note that the time-of-flight (TOF) detector was not included in this analysis due to technical limitations in the software. (These have since been removed.) The physics analysis was based on all global tracks which included i) refitted SVT-TPC matched tracks, ii) all remaining TPC tracks leftover after matching, and iii) most of the remaining SVT tracks which pass a chi-square cut (chi-square of circle fit less than 15.0).

The analysis was done assuming two configurations for the STAR detector. In the first, we assumed just the STAR baseline detector with TPC tracking only (*i.e.,* SVT physically removed from GEANT). In the second we additionally included the SVT. The same set of 100 central, Au+Au FRITIOF events at 100 A·GeV were analyzed for both detector configurations. In all the results shown here the pseudorapidity range considered for this analysis was $|\eta| \leq 1.5$.

At the time these calculations were done the SVT tracking algorithm was typically assigning several hundred low momentum ghost tracks per event while the TPC tracking code fragmented low momentum tracks into two or more separate tracks in many cases. (The former problem has been recently solved, but the latter remains). As a result the low transverse mass ($m_T \equiv \sqrt{m^2 + p_T^2}$) part of the reconstructed spectrum below 200 MeV was excluded from the temperature analysis. Since PID was based totally on dE/dx information, the analysis was also limited to $p < 600$ MeV/c.

Pion Temperature

In the analysis the pion distribution was assumed to be of the form

$$\frac{dN_\pi}{dm_T} = Am_T^2 e^{-m_T/T} \tag{11}$$

which best approximates that of a static fireball with equilibrium temperature T [12]. The above model adequately describes the FRITIOF primary pion spectrum and was sufficient for the present analysis. For actual data analysis, effects of flow and hadronic resonances must also be included. The temperatures of each of the 100 FRITIOF events were computed by fitting the function in Eq. (11) to the MC spectrum for primary pions from $m_T = 200$ to 1000 MeV. The pion multiplicity spectra were divided into 20 MeV bins in m_T. The fit quality, extracted temperature, and fitting uncertainty in T were not sensitive to moderate variations in the bin size away from 20 MeV. The resulting histogram is shown in Figs. 23 and 24 by the solid lines.

Before obtaining the temperature of the reconstructed pion distribution we first computed a multiplicity correction for pions based on the inclusive, summed MC and reconstructed pion spectra for all 100 events. The multiplicity ratio of MC to reconstructed pions as a function of m_T was computed and was found to be of order 1 and almost linearly dependent on m_T from 220 (240) to 800 MeV for the TPC only (SVT and TPC) configuration. This multiplicity correction was applied to each event and the corrected, reconstructed pion spectra were fitted using Eq. (11) from $m_T = 220$ (240) to 800 MeV for the TPC only (SVT and TPC) runs. The SVT ghost tracks contaminated the low momentum spectra, requiring the increase in the low m_T bound from 220 to 240 MeV for the SVT and TPC runs. The histograms of reconstructed pion temperatures are shown by the dashed lines in Figs. 23 and 24 for the TPC only and SVT-TPC calculations, respectively.

The correlations between input (MC) and output (multiplicity corrected - reconstructed) pion temperatures are shown in Figs. 25 and 26. Also shown are the typical fitting uncertainties for the temperature parameter T for the MC and reconstructed spectra. The error in the fits to the reconstructed spectra (about 4 MeV) is larger than that for the MC (about 3 MeV) due to the smaller, restricted m_T range used in the former. The scatter in the points in Figs. 25 and 26 is consistent with these fitting errors. In this analysis all 100 events had basically the same pion temperature. Therefore, a dramatic input-output correlation plot should not be expected. Analyses with many events spanning a wide temperature range remains to be done. The reconstructed temperature for the SVT-TPC runs is also about 5 MeV lower, on average, than for the TPC only runs. This demonstrates the sensitivity of the extracted temperature to the assumed m_T range.

The σ's of the reconstructed temperature distributions in Figs. 23 and 24 are about 4 MeV, consistent with the typical fitting error for each event. Extraction of kaon and proton temperatures was attempted but was unsatisfactory with the present analysis software which did not include PID using the TOF.

Pion Mean p_T

Shifts in the mean p_T for pions is predicted to be an important indicator for interesting phenomenon such as disoriented chiral condensates (DCC) [9] in the QGP. The histograms of the mean p_T for pions (using all tracks with momenta from 0-2 GeV/c and no multiplicity corrections) for the 100 MC and reconstructed events are shown in Figs. 27 and 28 for the TPC only and SVT-TPC cases, respectively. The systematic shift to lower $\langle p_T \rangle$ for the reconstructed events is a result of the SVT ghost track and fragmented TPC track problems for the low momentum tracks. The width of the reconstructed pion $\langle p_T \rangle$ distribution is similar to that for the MC, σ being about 7 MeV/c, and is little affected by the SVT. Large DCC domains are expected to produce shifts in $\langle p_T \rangle$ of order 5 MeV/c or less however [13].

K/π Ratios

K/π and $p/\bar{p}$ ratios were calculated for MC and reconstructed events (no multiplicity corrections) for the following p_T ranges: < 200 MeV/c, $200 \leq p_T \leq 400$ MeV/c, $400 \leq p_T \leq 600$ MeV/c, and > 600 MeV/c. Figs. 29 and 30 show the histograms of K/π ratios for the 200 to 400 MeV/c and 400 to 600 MeV/c ranges for the 100 TPC only and 100 SVT-TPC calculations, respectively. Outside this p_T region the reconstructed K/π ratio fails to reproduce the MC, while inside the range, good agreement was achieved between the reconstructed and MC results. The mean of the reconstructed K/π ratio distributions is increased towards the MC value when the SVT is included. It has been observed in previous analyses that the reconstructed K/π ratio is improved, with respect to the MC value, for the subset of matched SVT-TPC tracks. The σ's of the MC and reconstructed (TPC only or SVT-TPC) distributions are similar, being about 0.009 (0.02) or about 15% (20%) of the mean K/π ratio in the 200-400 MeV/c (400-600 MeV/c) range. The reconstructed $p/\bar{p}$ ratio did not reproduce the MC ratio very well in any p_T range, given the present analysis software with the TOF not included, and hence was not included here.

Summary and Conclusions

In summary, this event-by-event analysis of reconstructed pion and kaon tracks with the TPC only and the SVT-TPC configurations of STAR indicates the following: (1) the single event pion temperature can be measured to about ± 4 MeV, (2) systematic shifts in extracted temperature relative to the MC temperature can mostly be removed from the analysis by straightforward multiplicity corrections,

(3) the single event pion $\langle p_T \rangle$ can be determined to about ± 7 MeV/c, (4) systematic error in the extracted $\langle p_T \rangle$ is large, at present, due to problems with the low momentum tracking algorithms, (5) the K/π ratio is well reproduced in the 200 - 600 MeV/c range with the single event σ being 15-20% of the mean K/π ratio value, (6) the reconstructed single event $p/\bar{p}$ ratio is not satisfactory at present, and (7) the SVT does not significantly affect these specific event-by-event observables. However, recent improvements in the SVT tracking algorithm remove most of the low momentum SVT ghost tracks and should enable measurements using the SVT to extend the event-by-event quantities discussed here to lower m_T ranges below 200 MeV where the possibility of discovering interesting, new physics awaits.

This research was supported in part by the U. S. Dept. of Energy under grant No. DE-FG03-94ER40845 and by The Robert A. Welch Foundation.

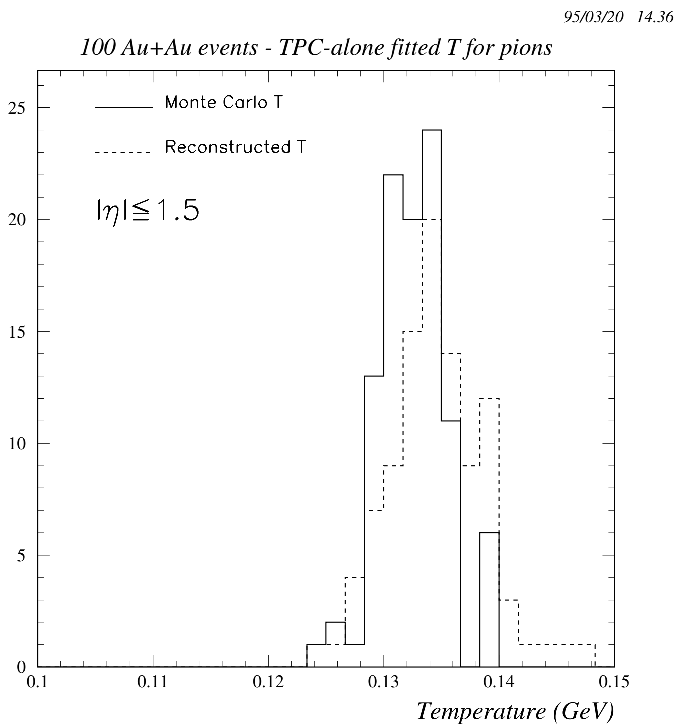

Figure 23: Pion temperature distribution

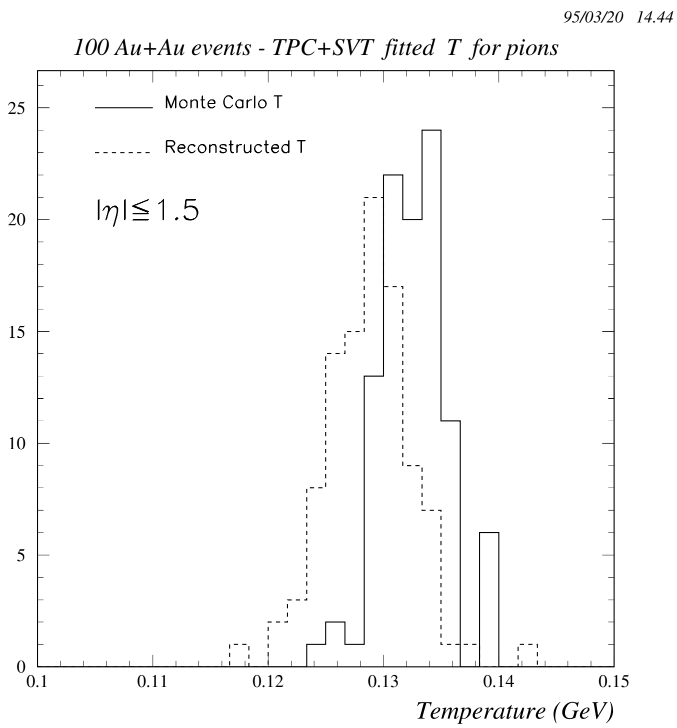

Figure 24: Pion temperature distribution

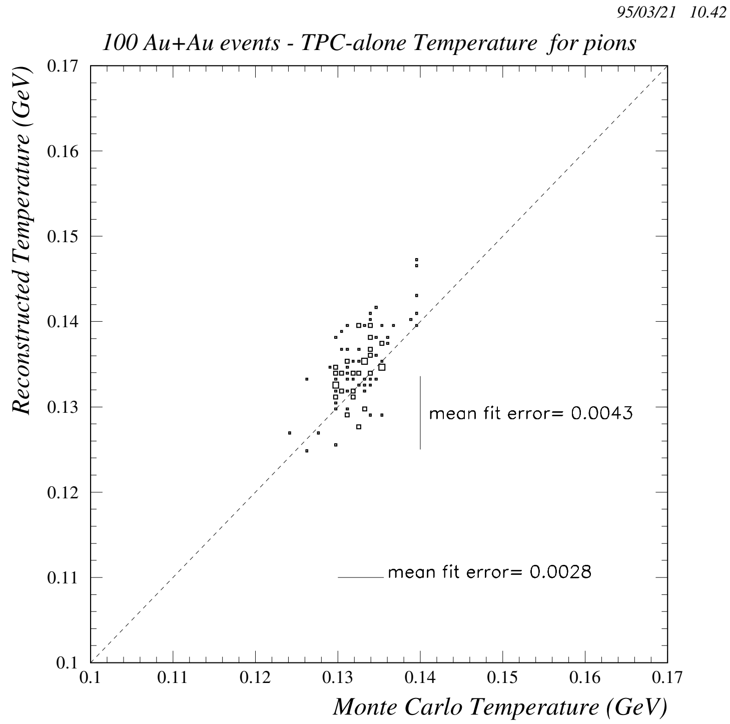

Figure 25: Correlation between reconstructed and Monte Carlo temperatures.

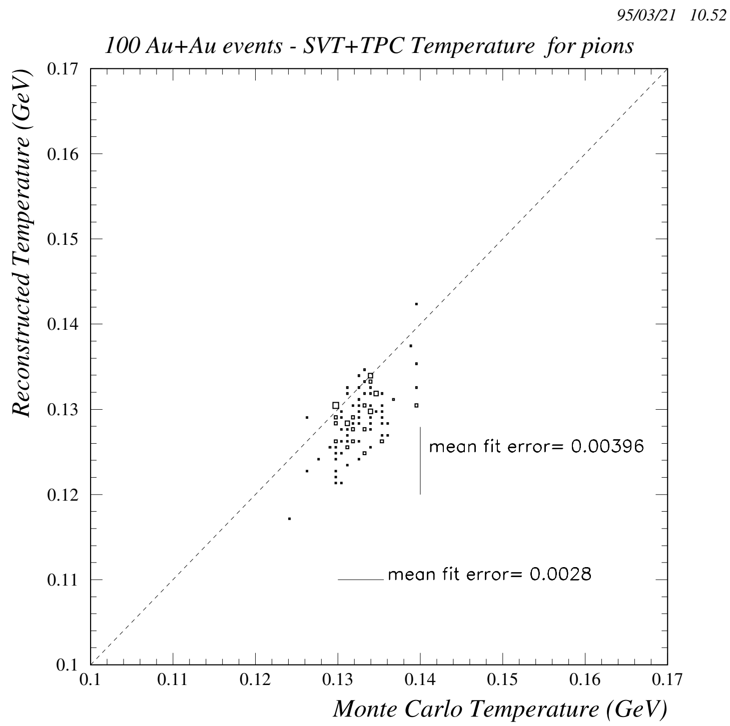

Figure 26: Correlation between reconstructed and Monte Carlo temperatures.

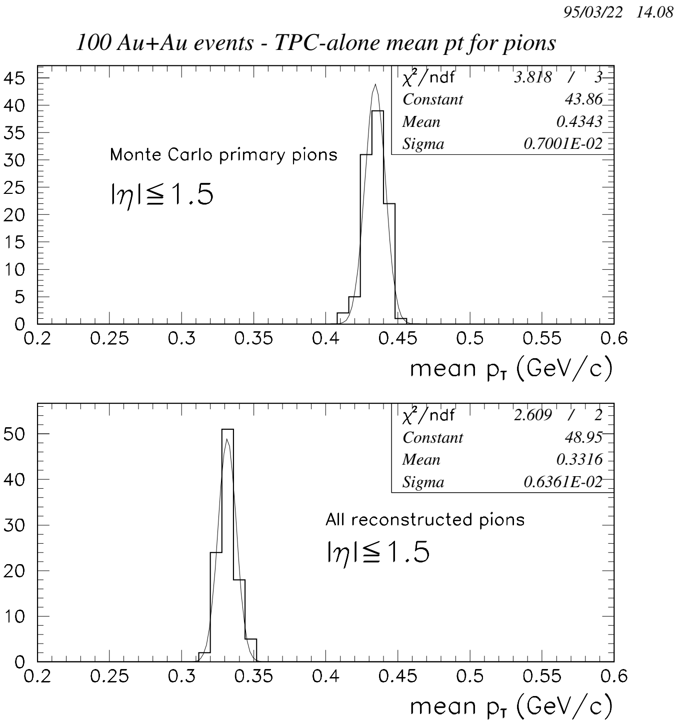

Figure 27: Mean p_T distribution for pions

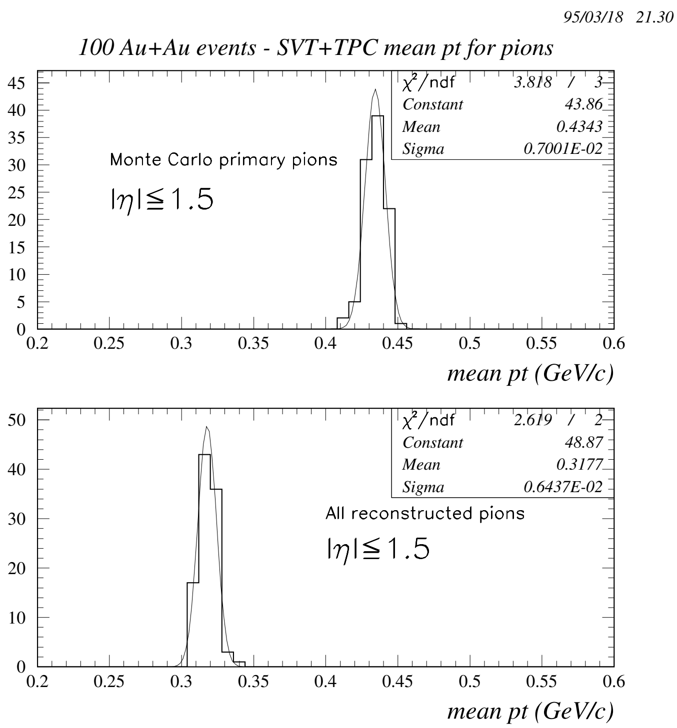

Figure 28: Mean p_T distribution for pions

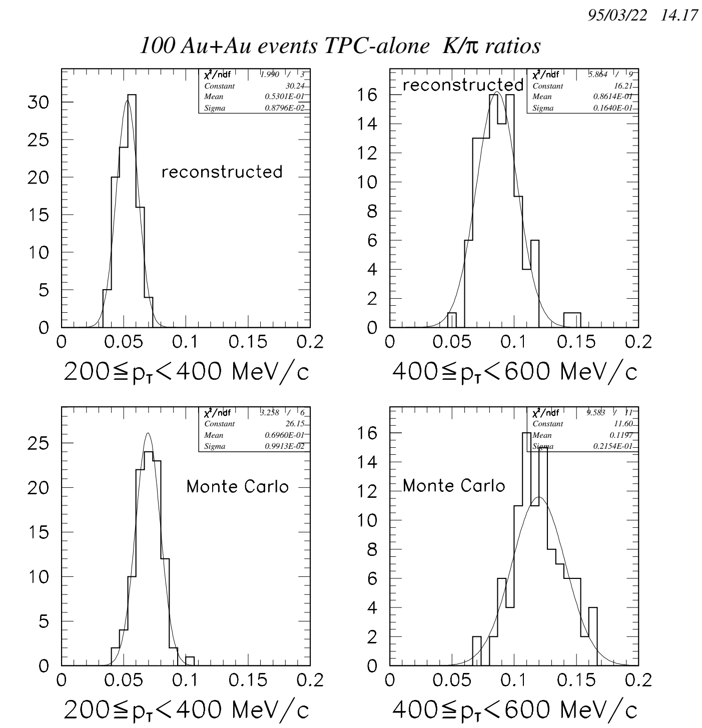

Figure 29: K/π ratio in the p_T ranges from 200 to 400 MeV/c and from 400 to 600 MeV/c.

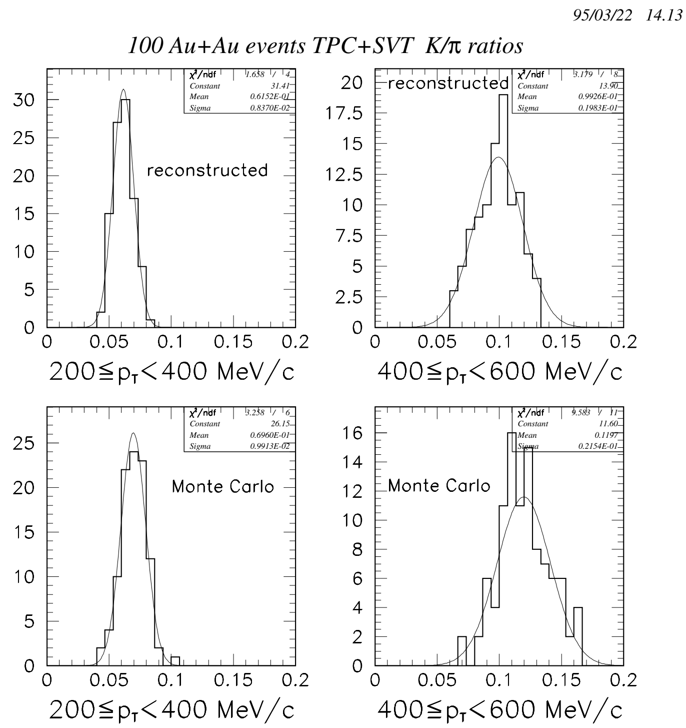

Figure 30: K/π ratio in the p_T ranges from 200 to 400 MeV/c and from 400 to 600 MeV/c.

3.2 Efficiency of Modified UA1 Jet Reconstruction Algorithm in pp, pA and AA Collisions at STAR

Contributed by: B. Christie and K. Shestermanov

Introduction

The efficiency of a modified *UA1* jet reconstruction algorithm, and the reconstructed jet's p_T resolution in pp, pA and AA events using the STAR detector was studied. The HIJING and PYTHIA event generators, full GEANT simulations and the Time Projection Chamber (TPC) Analysis Shell (TAS) was used.

Detector

The STAR detector at RHIC has been described elsewhere [14],[15]. The proposed barrel electromagnetic calorimeter EMC [15] is a lead scintillator sampling calorimeter. It covers $|\eta| \leq 1.05$ and 2π in azimuth, thus matching the full tracking acceptance of the TPC. The EMC segmentation is $\Delta\eta \times \Delta\phi = 0.1$ and it consists of 1200 towers.

Event simulation

The HIJING [16] event generator has been used for pp, pAu, CC, OO, $SiSi$ and $FeFe$ collisions. In order to compare the jet properties, pp events were also simulated using PYTHIA V5.702/JETSET V7.401 LUND programs [17].

For the purposes of this study it was desirable to separate the acceptance of the EMC barrel from the efficiency of the jet finding code. We accomplished this by calculating the pseudorapidity of the two scattered partons as the events are generated by the HIJING event generator code, and only writing out those events for which the scattered partons lie within a prescribed region. For all the results presented in this report both of the hard scattered partons were produced within $|\eta| \leq 0.3$.

The initial conditions and kinematics of events of interest were the following:

- $\sqrt{s} = 200$ GeV;

- the impact parameter varied from 0 to 0.75 fm for pAu and AA collisions;

- the p_T of the scattered parton, p_T^{parton} was assumed to be 10, 15, 20 and 30 GeV/c for pAu and 30 GeV/c in pp and AA collisions;

- the η_{min} and η_{max} for high $p_T^{partons}$ were -0.3 and $+0.3$.

The number of events analyzed for each sample of pp or AA collisions was about 100 and was limited by the GEANT computing time and the size of the files created. For example, the processing of 75 $FeFe$ events took about 50 hours of cpu time on the RSGI00 processor with 10.5 $Mflops$ and the size of the output files was about 0.3 $Gbyte$.

TAS modules for STAR EMC

The package *ems* (Electro Magnetic Simulation) and the corresponding documentation were created by B. Christie. The brief description below is extracted from the World Wide Web *WWW* system of STAR, (STAR → STAR news → EMC news → TAS *ems* modules). There are three TAS modules in the *ems* package presently:

1. *ems_tot.F* is the first module called in the *ems* package. It reads in the EMC hits table, which is filled by the TAS module *mct*, sums up the energy deposited in each of the towers, and fills the output table EMS_HITS_V. The input table from *mct* contains the GEANT "hits" bank information for every charged particle which crosses any plastic layer in the STAR EMC.

2. *emc_egrid.F* is the second module called in the *ems* package. This module reads in the output table of *ems_tot.F* and the global track table output from the tracking package *egr*. For each "good" track in the global track table, this module projects the track to see if it hits the barrel EMC. If so, a parameterized amount of energy ($f(\mid P \mid)$) is subtracted from the struck tower. The track is then projected in the other direction to the point of closest approach to the primary vertex. At present the primary vertex is assumed to be at coordinates 0,0,0. The track's total energy is evaluated at this point, assuming that it is a pion, and this "charged" energy is put into the appropriate $\eta - \phi$ bin. After this the energy remaining in the EMC barrel is multiplied by 1/sampling factor (= 16.00) to give the deduced neutral energy incident on the EMC. This factor of 16.00 is set via a data statement in the module. The output table for this module is named EME_COR.

3. *erj_bar.F* is the third module called in the *ems* package. This module contains the modified (by K. Shestermanov) *UA1* jet finding code. This module reads in the output table of the *emc_egrid.F* module described above.

Results

The modified *UA1* algorithm [18],[19],[20] has been used for jet finding. This is a cone type algorithm, and it has 3 parameters:

- The tower threshold for seed transverse energy, E_T^{seed};

- The jet cone radius in $\eta - \phi$ plane, R_0;

- The threshold for jet energy, E_j.

For our study the algorithm was modified in order to suppress the background from soft interactions in AA collisions. It proceeds through the following steps:

1. Each cell in the energy histogram $\eta - \phi$ is assigned an energy vector whose magnitude is given by the energy deposited in the cell, E_T, and whose direction is given by the center of the cell.

2. The average transverse energy per cell, E_{back}, is calculated ($E_{back} = \frac{1}{n} \sum_{i,j} E_{i,j}$, where n is the number of cells). This value is then subtracted from each cell.

3. All cells with $E_T > E_T^{seed}$ are ordered in decreasing transverse energy.

4. The cell with the highest transverse energy initiates the first jet.

5. Cells are added vectorially to the first one if they are within a distance R_0 (in $\eta - \phi$ space) from the center of a cone at the cell with the highest E_T. A jet momentum vector is defined as the vectorial sum of all individual cells within the cone of radius R_0. The center of the cone is then recalculated in the direction of the reconstructed jet momentum. This procedure is repeated until the distance between the 'old' and 'new' center of the cone becomes less than $0.05R_0$.

6. If the next seed cell is outside this radius then a new jet is initiated. This procedure is repeated until all cells above E_T^{seed} threshold are assigned to jets.

7. If the jet energy is greater than E_j the jet is accepted.

8. The value E_{back} of the background E_T energy is then recalculated using only remaining cells not assigned to the jets, and the jet finding iteration is repeated.

This algorithm converges in three-four steps.

The efficiency of two jet finding is defined as

$$Eff = N_{dijets}/N_{dipartons} \, ,$$

where N_{dijets} is the number of events with two jets and $N_{dipartons}$ is the number of generated events with two high p_T partons with the kinematics described earlier.

The jets were considered to be found if the back-to-back ϕ deviation for the two jets did not exceed 30°, and the jet's energy was greater than 10 GeV (N.B. this cut is only used for the study of 30 GeV jets). We checked the angular correlation between the scattered partons and the reconstructed jets. In the case of pp the average value for the deviation in ϕ was $\simeq 5°$. In *FeFe* the average value for this deviation was $\simeq 13°$.

The results for efficiencies and for the RMS p_T^{jet} value for $R_0 = 1$, $E_j = 5\,GeV$ ($E_j = 9$ GeV in *FeFe* collisions) and $E_T^{seed} = 1.0$ GeV are presented in Table II and Fig. 31.

Interaction	Efficiency, %	$RMS\ p_T^{jet}$, %
pp(HIJING)	78.9 ± 8.0	24.1
pAu	63.8 ± 7.8	30.8
CC	65.8 ± 6.5	30.4
OO	70.7 ± 7.3	30.3
$SiSi$	61.3 ± 9.0	30.9
$FeFe$	47.9 ± 7.1	38.7

Table II: Efficiencies and $RMS\ p_T^{jet}$.

The distribution of the differences between p_T^{parton} and p_T^{jet} in pp, pAu and AA collisions are shown in Figs. 32.2 - 32.7. Note that the mean of the distributions of $p_T^{parton} - p_T^{jet}$ get more positive as the size of the colliding systems increases. This may be a consequence of the jet quenching mechanism in HIJING. This jet quenching leads to a softening and broadening of the fragmentation function via induced gluon bremsstrahlung for the high p_T partons. As the fragmentation function broadens more of the jet's energy falls outside of the fixed cone radius used in the jet algorithm. This is consistent with the trend shown in Figs. 32.2 - 32.7. We will investigate this further by generating events with the jet quenching feature turned off in HIJING.

The results for efficiencies and for the $RMS\ p_T^{jet}$ values as a function of p_T^{jet} in the pAu collisions are presented in Fig. 33 for $E_T^{seed} = 0.5$ GeV, $E_j = 3$ GeV, and the same demands for angles in the x-y plane. No additional cut for the jet's energy was applied.

To determine quantitatively how the finite resolution, tracking efficiency, and pixelation of the STAR detector affects our jet finding efficiency and resolution, the jet finding algorithm was run directly on the output of the event generators. In this study the jet direction was taken to be the direction of the scattered parton, as given by the event generator. The energy of all particles in the event generator output file (excluding neutrinos) which were within the cone radius of the parton was summed to get the jet energy. The results for pp collisions ("ideal") are presented in Table III.

From this table one observes that the data for both STAR and the "ideal" detector are quite close to one another. The small differences observed are primarily due to the inefficiency of the STAR detector to the neutrons and K_L^0 mesons, and also from the finite resolution and granularity of the STAR calorimeter.

Much more significant are the differences of the angles between the parton and jet axis for the events generated with HIJING and PYTHIA. The HIJING events show a much wider distribution for this quantity than the PYTHIA events. It is important that we understand the reason for this difference as it has a direct impact on our resolution of the Bjorken x values in our analysis.

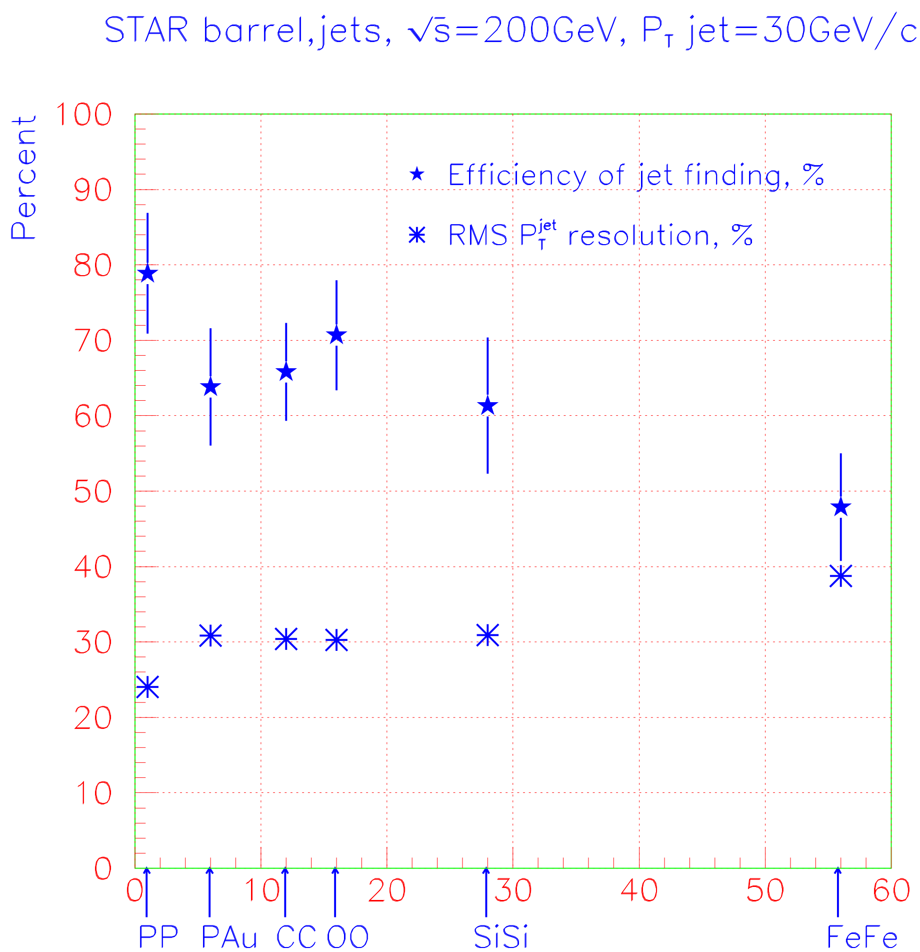

Fig. 1

Figure 31: Efficiency of finding dijets and RMS p_T^{jet} resolution in pp, pAu and AA interactions.

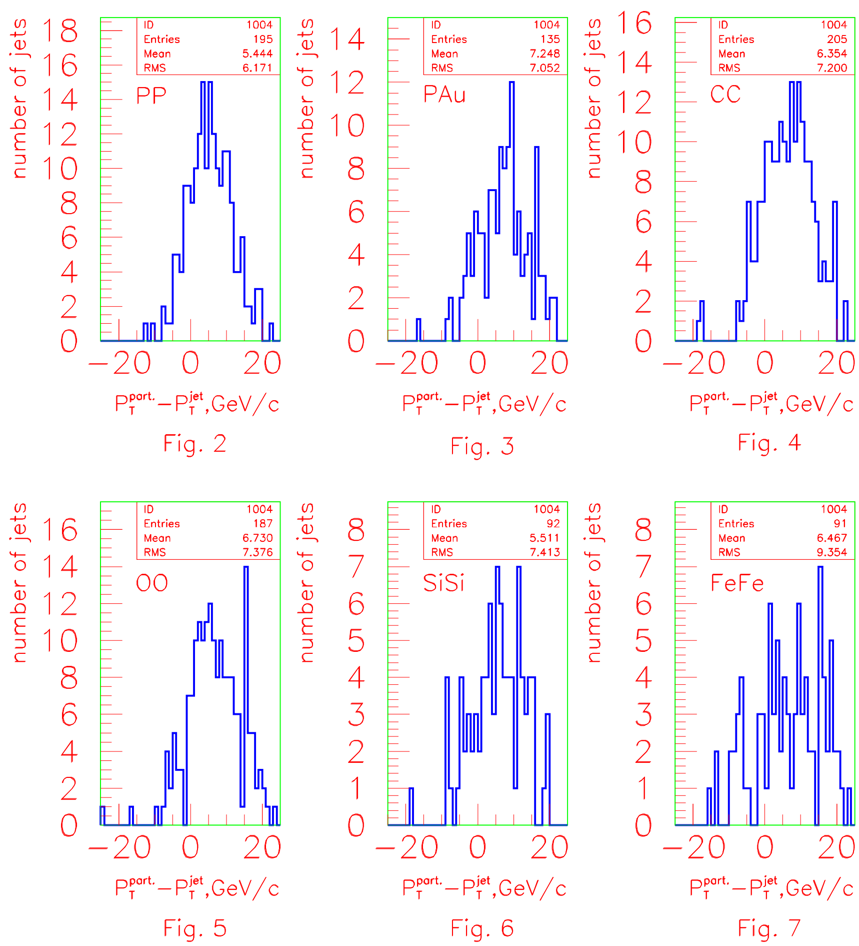

Figure 32: Part 2: $p_T^{parton} - p_T^{jet}$ distribution in pp interactions. Part 3: $p_T^{parton} - p_T^{jet}$ distribution in pAu interactions. Part 4: $p_T^{parton} - p_T^{jet}$ distribution in CC interactions. Part 5: $p_T^{parton} - p_T^{jet}$ distribution in OO interactions. Part 6: $p_T^{parton} - p_T^{jet}$ distribution in $SiSi$ interactions. Part 7: $p_T^{parton} - p_T^{jet}$ distribution in $FeFe$ interactions.

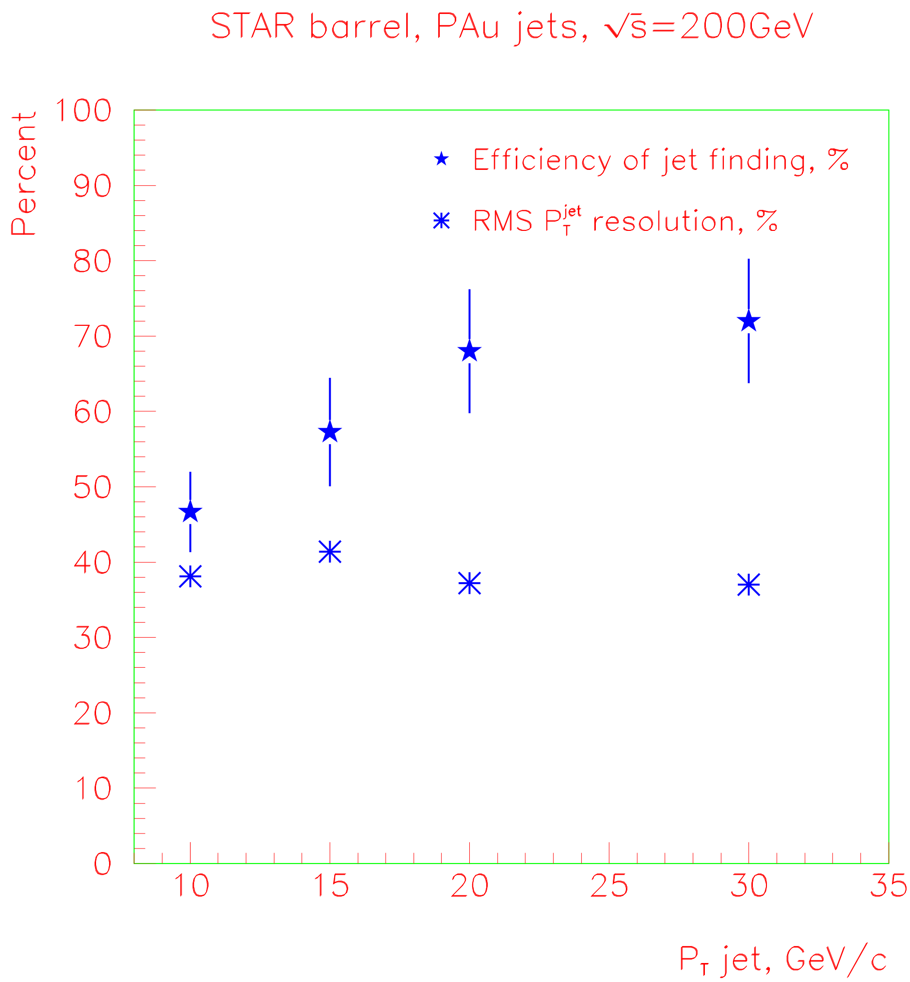

Fig. 8

Figure 33: Efficiency of finding dijets and RMS p_T^{jet} resolution in pAu interactions as function of p_T^{jet}.

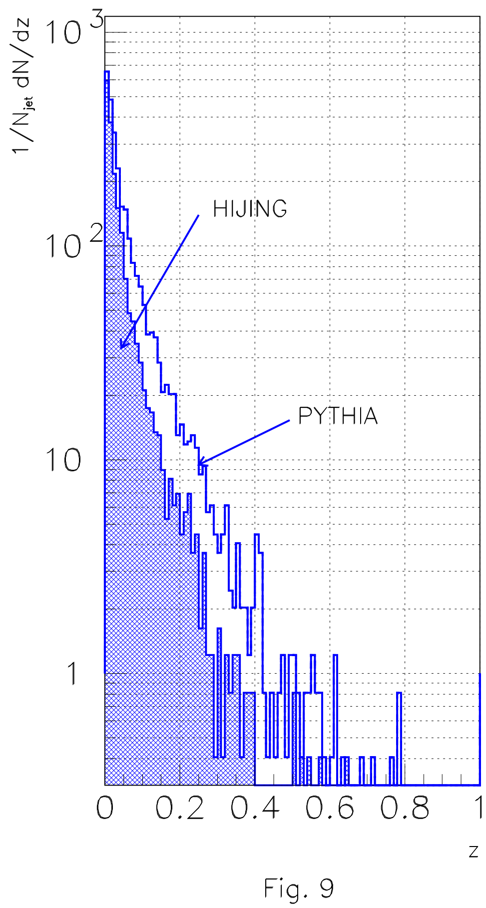

Figure 34: Charged-particle fragmentation function for $p_T^{jet} = 30$ GeV/c in pp interactions for HIJING (shadow) and PYTHIA event generators.

	HIJING		PYTHIA	
	"ideal"	STAR	"ideal"	STAR
Efficiency, %		78.9 ± 8.0		91.9 ± 8.6
p_T^{parton} (RMS), GeV/c	30.3(2.4)	30.3(2.3)	30.5(1.5)	30.4(1.6)
p_T^{jet} (RMS), GeV/c	25.2(5.5)	24.8(5.9)	26.6(4.1)	26.7(6.3)
Angle in y-z plane (RMS) ,degrees	11.5(11.8)	13.6(14.6)	3.1(5.0)	3.9(6.5)
Angle in space (RMS) ,degrees	13.8(12.0)	16.1(15.3)	4.9(7.4)	6.5(10.2)

Table III: Parameters of jets from different event generators in pp collisions.

For comparison purposes we empirically extracted the charged particle fragmentation function for the HIJING and PYTHIA event generators. One can see this in Fig. 34, where the charged particle fragmentation functions for $p_T = 30$ GeV/c jets are shown as a function of the inclusive variable [21]

$$z = P_l^{\pm}/E_{parton} ,$$

where $P_l^{\pm}$ is the momentum of the charged particle projected on the parton axis, and E_{parton} is the energy of the parton.

Conclusion

It has been shown that the modified *UA1* jet finding algorithm can be used with reasonable efficiency for jet reconstruction in the central η region in pp, pA, and heavy ions collisions. Still to be understood and resolved is some inconsistency of the characteristics of the pp events produced by the HIJING and PYTHIA/JETSET generators.

The discussions with A. Yokosawa, J. Carroll, G. Westfall, D. Underwood, T. Hallman and V. Rykov were extremely helpful. We appreciate all of them.

3.3 High p_T Physics with the TOF

Contributed by: Stathes Paganis and Pablo Yepes

Physics Motivation

The search for the Quark Gluon Plasma (QGP) is one of the main purposes of the Relativistic Heavy Ion Collider (RHIC) being built at BNL. An intense research program has recently been carried out in relativistic heavy ion collisions, and a number of QGP signatures have been proposed. Some of these signatures, like strangeness enhancement and J/Ψ suppression, were observed experimentally. After the initial excitement created in the community by these observations, many models that do not include QGP formation were shown to explain the data. As a consequence, the importance of understanding the properties of the hadronic matter, before making any statements concerning the creation of the QGP, was realized. The determination of the temperature, density, transverse and longitudinal flow and source volume reached in the collision are essential ingredients to understanding the dynamics of the hadronic matter.

Transverse Mass

The temperature of a static, thermalized particle source can be obtained from the $(1/m_T)dn/dm_T$ distribution of the emitted particles. This simple picture is modified in reality by the presence of resonances and transverse flow. Resonances tend to modify the m_T spectrum at low momentum, especially for light particles, like pions, while transverse flow increases the transverse mass. In this context, the measurement of the m_T spectrum for pions, kaons and protons in a large m_T range is very important in order to understand the characteristics of the hot hadronic matter produced after the collisions of heavy ions for pions, kaons and protons in a large m_T range [22].

In STAR, the meaningful m_T range for pions, kaons and protons in which precise measurements are available is extended significantly by the inclusion of the TOF system. This is illustrated in Fig. 35, where $(1/m_T)dn/dm_T$ is plotted for the different particle species with and without the information provided by the TOF system. As is apparent from this figure, the TOF system expands the measurable range of m_T considerably. It is important to note that the slopes of these distributions vary with m_T. The temperatures extracted from the inverse slopes of these distributions may therefore be difficult to interpret in the absence of the TOF information.

Particle Correlations

Particle correlation measurements have been widely used to extract the source size at freeze-out. Most often pions are used to form the interferometric correlation functions. However, the presence of abundant resonances tends to distort the source radius extracted from the pion correlation for low momentum pairs. The situation improves when analyzing kaon correlations and/or high momentum pairs.

Kaon interferometry has been used to deduce the size of the kaon emitting source. Kaon correlations are less affected by resonances and the lifetime of the source can be extracted from them [23]. In addition, the study of interferometry as a function of transverse momentum provides useful information about particle flow. The presence of QGP droplets in hadronic matter has also been predicted to produce characteristic features in the kaon correlation function [24]. The presence of the TOF system will significantly extend the p_T range where kaon interferometry can be studied.

The enhanced capability of STAR with TOF for studying kaon interferometry has been investigated using the full Monte Carlo simulation for STAR. Special events with 1000 correlated kaon pairs with a flat p_T distribution and a momentum difference between 0-300 MeV/c were generated and run through the Monte Carlo and event reconstruction analysis chains.

The correlation distribution was studied as a function of $Q = \sqrt{-qq}$, where q is defined as $q \equiv q_1 - q_2$, where q_i is the four-momentum of particle i, i=1,2. The uncorrelated distribution was built using tracks belonging to different events. The correlation function was obtained by dividing the correlation distribution by the uncorrelated one.

Figure 36 shows the correlation functions obtained after reconstruction in different bins in p_T of the particle pair. Without the TOF system only pairs with p_T below 1 GeV can be reconstructed. With the TOF the correlation function can be obtained in different p_T bins as shown in the plot. The width of the reconstructed correlation function increases when going to large p_T, reproducing the behavior of the input correlation function.

Strangeness Enhancement

The K/π ratio does not by itself provide a signature for QGP formation. However, it has been proposed that the variation of this ratio with temperature and chemical potential in the presence of a QGP could be unique [25]. A very precise study of the ratio as a function of transverse momentum, which can only be achieved with the information of the TOF system, will shed light on the origin of possible enhancements to this ratio.

The production cross section of the ϕ-meson can be measured inclusively from the decay $\phi \rightarrow K^+K^-$. The measurement of the yield of the ϕ, which is an $s\bar{s}$ pair, places more stringent constraints on the origin of the observed flavor composition than the K/π ratio. The production rate is also expected to be extremely sensitive to changes in the quark masses [26], due to the chiral transition at high energy densities which is predicted by lattice QCD calculations. Moreover shifts in the ϕ-meson mass and width have been predicted in a hot hadronic medium [27]. In fact the E859 Collaboration has reported a shift in the ϕ-meson as a function of reaction centrality [28]. In order to understand these effects a careful and systematic study of ϕ production is needed. The particle yield as a function of p_T is one of the most basic tools to understanding the production mechanism of any particle.

The ϕ p_T distribution with/without the proposed TOF system is shown in Figure 37. As can be observed, studying the p_T dependence without the TOF system appears to be problematic.

Jet Quenching

When the QGP is formed in a heavy-ion collision most of the particles produced in this new state of matter must undergo freeze-out and hadronization processes before reaching the experimental apparatus. Unfortunately, most of the particles that are detected may have lost all memory of the primordial QGP. In principle, only jets and leptons are predicted to retain any memory of the transient QGP. The study of jets is interesting since RHIC will be the first heavy ion machine with a high enough energy to produce them. However, the experimental challenges that jet detection presents in AuAu collisions are substantial.

The TOF system can provide a unique tool to study jet quenching by measuring the ratio of high p_T proton/antiproton spectra. Protons are mainly produced in quark jets, while antiprotons are predominantly generated in gluon jets. Since gluons lose more energy in the QGP than quarks, p and $\bar{p}$ should be affected differently. Therefore, modified p_T spectra are expected [29]. This effect is illustrated in Figure 38 obtained with the Monte Carlo program HIJING which includes a jet quenching algorithm [30]. The plot shows the ratio

$$(dn/dp_T)_{AuAu}/(dn/dp_T)_{pp}$$

for protons and antiprotons with and without jet quenching, where $(dn/dp_T)_{AuAu}$ and $(dn/dp_T)_{pp}$ are the number of particles produced in central AuAu and proton-proton collisions, respectively. Jet quenching is reflected mainly in the antiproton ratio.

Other mechanisms due to the presence of QGP have also been proposed for the suppression of high p_T nucleons [31]. Processes have been predicted to suppress intermediate-p_T antiproton production in heavy ion collisions. This could be used as a probe of the space-time evolution of the reaction [32]. The TOF system will allow the study of such antiproton spectra, which are potentially very interesting.

Open Charm

The possibility of using the TOF in combination with a vertex detector is investigated in this section. $D^0(D^{\pm})$ meson branching ratios for decays into charged kaons is around 50%(30%). Due to the high mass of the D-mesons these daughter kaons tend to have large p_T. In the present STAR design only the TOF will be able to identify them.

Kaons produced in a sample of 850 HIJING central AuAu collisions were selected and split into primaries and secondaries from charm meson decays. These were run through the full Monte Carlo and simulation chains. The present study considers a production of 1(0.5) $D^0(D^{\pm})$ per unit rapidity.

The minimum distance between the reconstructed tracks and the main vertex was calculated for both kaon samples. We will refer to this quantity as the *offset*. Because of technical difficulties a vertex gas detector was consider instead of the SVT. The main difference between these detectors is the very low multiple scattering in the gas detector. However this difference should be less significant for high momentum particles.

Figure 39a and b show the offset distribution for kaons with no p_T cuts and with p_T >1.3 GeV/c, respectively. As can be seen the use of a high p_T cut reduces the background from primary kaons by nearly two orders of magnitude. This cut in high p_T kaons **can only be achieved with the TOF system**. When high p_T kaons are used a signal to background ratio of 1/4 is obtained for particles with an offset larger than 300 microns. These results indicate that a D-meson production measurement might be possible using the TOF system combined with a light vertex detector. Even if the results look promising, a careful understanding of the tail will be necessary with real data. However such an understanding at the level of 10% should be achievable by comparing different reactions, like pp, SiSi, AuAu, etc. Nevertheless further studies are necessary to reach a more definite conclusion.

This research was supported in part by the U. S. Dept. of Energy under grant No. DE-FG03-94ER40845 and The Robert A. Welch Foundation.

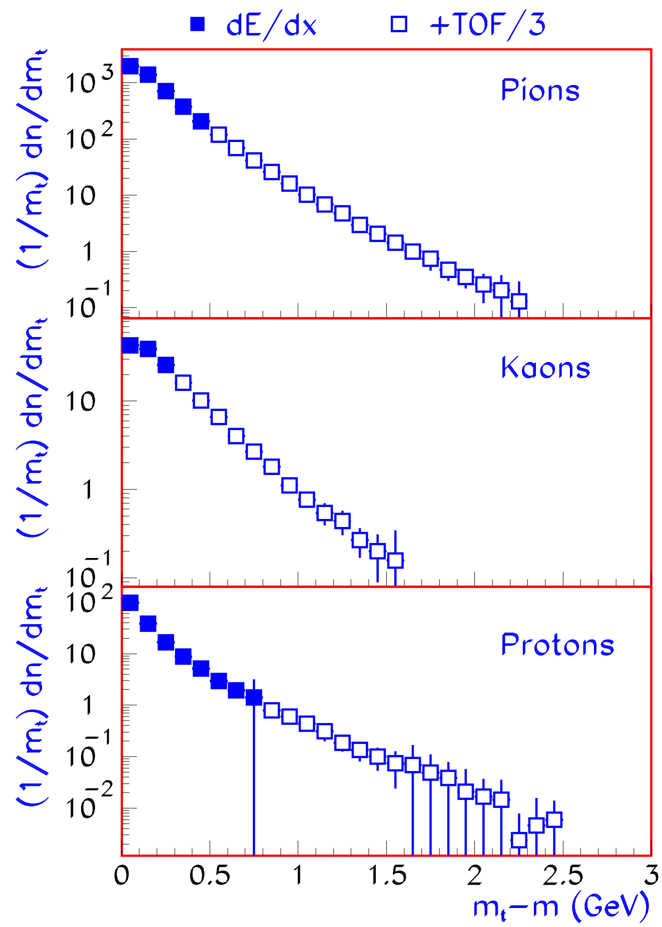

Figure 35: Invariant cross sections versus the transverse mass for pions, kaons and protons from the full simulation of the STAR detector for central AuAu collision using the HIJING model for particle production. The shaded points show the region that can be measured using only dE/dx from the TPC for PID. The open points are obtained with inclusion of the TOF system.

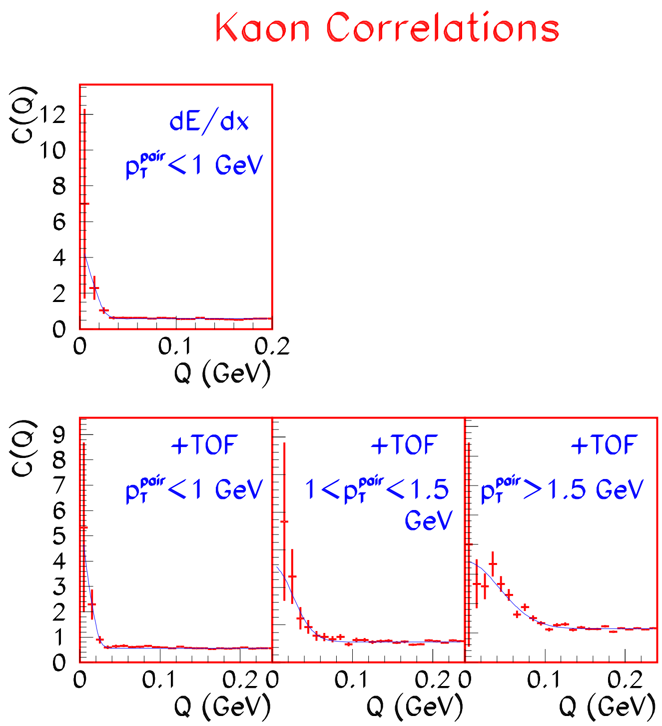

Figure 36: Kaon correlation functions in three p_T^{pair}, (transverse momentum of the particle pair) bins from the full simulation of the STAR detector using special events with correlated kaons for particle production. Correlations with $p_T^{pair} > 1$ GeV cannot be obtained with only the TPC. The upper plot is obtained using only the dE/dx from the TPC for PID. The lower plots are obtained with inclusion of the TOF system.

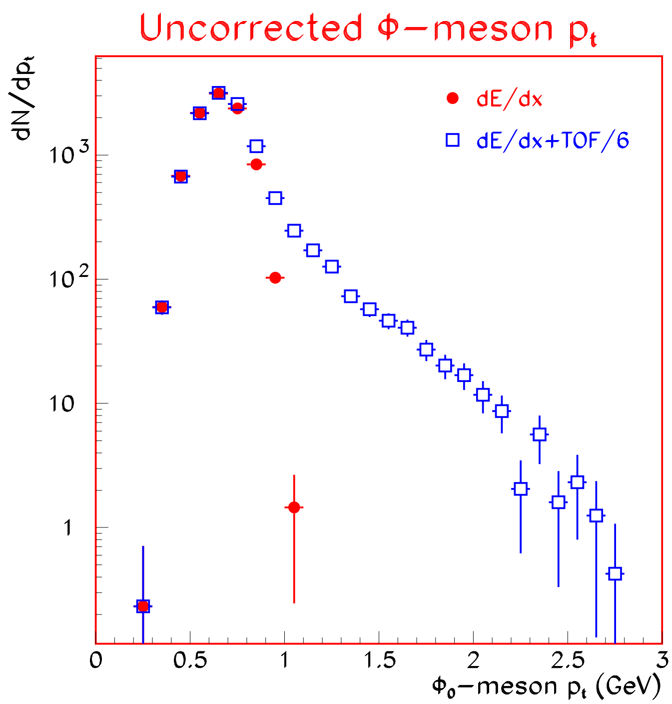

Figure 37: The ϕ meson p_T spectrum using only dE/dx from the TPC (solid points), and including a one-sixth patch of the TOF system (open points). The distributions are not corrected for the detection efficiencies or the geometrical acceptance.

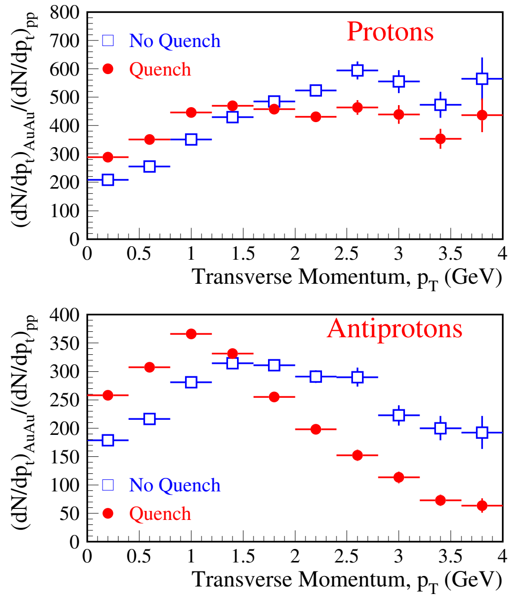

Figure 38: Particle production ratio in central AuAu relative to proton-proton collisions as a function of p_T for protons and antiprotons obtained using HIJING with (solid circles) and without (open squares) jet quenching.

3.4 Event-by-Event Physics at $|\eta| > 2$

Contributed by: Daniel Cebra

Introduction

In this simulation we study the event-by-event physics capabilities of the STAR XTPC system which can result from analysis of charged particle multiplicity distributions, $(+)-(-)$ charge particle distribution differences, and slopes of p_T distributions (temperature), all at pseudorapidity greater than 2. The XTPCs for STAR allow characterization of an individual event in terms of temperature variations with η, stopping, and baryon flow.

Recently RHIC management has been asked to defend the items which have been included in the Additional Equipment Request. This defense took place at BNL on January 4th and 5th, and the XTPC (external time projection chamber) project was one of the items which was presented to the NSAC subpanel for consideration. At that review the panel questioned why a device like the XTPC would be needed. It was suggested that the inclusive data would be better taken by a small solid angle spectrometer like BRAHMS, which RHIC was already determined to build. It was further suggested that the exclusive data did not need the tracking information that the XTPCs provide, and that PHOBOS could do all the exclusive work with simple, and inexpensive pixel detectors. The XTPC group believes that these would not be the appropriate conclusions, and the reasons for this belief are given in this paper.

Originally, the XTPC group had planned to address the question of the physics accessible with a detector which had broad tracking coverage, such as the combined central TPC and XTPCs would provide for STAR. The goal would have been to emphasize the strength of the approach that STAR has taken as its central philosophy - complete coverage (at least of the charged particles). With the inclusion of the XTPCs, STAR reconstructs over 90% of all charged particles, without them the fraction is about 50%, which would leave much of the reaction unobserved. It also leaves the forward regions completely uncharacterized. It is important to understanding the collision/fragmentation process to be able to measure the transition of thermodynamic variables from the *HOT* mid-rapidity regions into the *cold* fragmentation regions at high η, on an event-by-event basis.

However, we were unable to present such a global analysis, because, as yet, there exist no simulations data that adequately incorporate the central TPC and the XTPC simultaneously. The high η region is not only technically demanding on detection instrumentation, but it is also computationally demanding on the software. That is, it is necessary to run GEANT with a realistic magnetic field map (not just a pure, constant, axial field) to provide meaningful simulations for the XTPC, while for the remainder of STAR, it has not yet been necessary to incorporate the realistic magnetic field into the simulations. We therefore have good simulations data only for the XTPC alone, with the rest of STAR considered simply as a source of MCS and background.

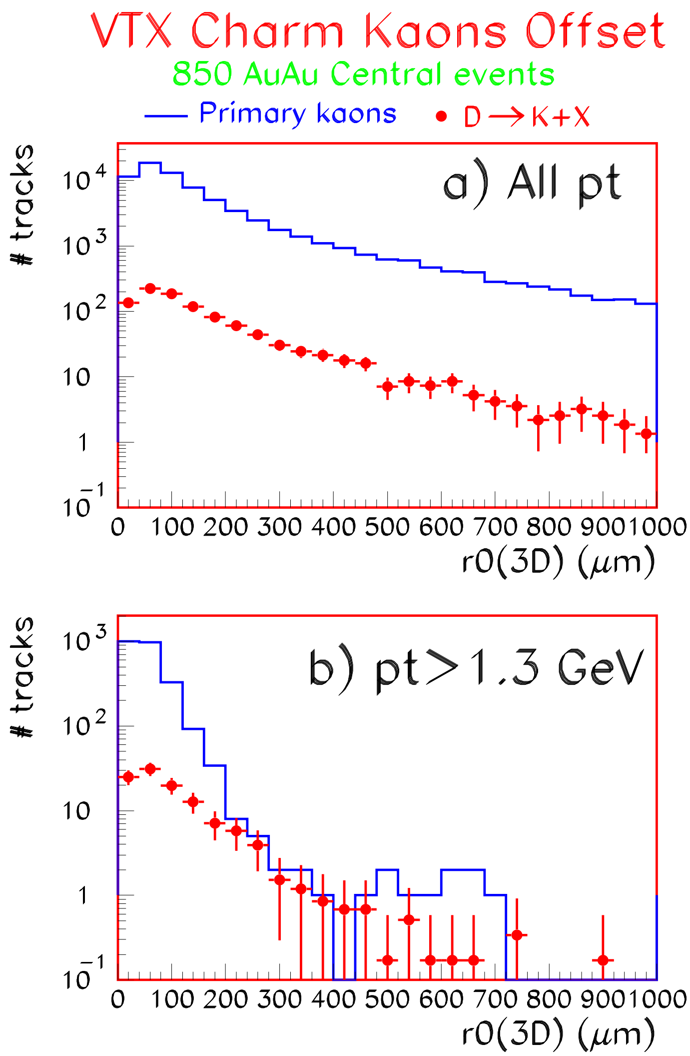

Figure 39: Offset distributions of primary kaons and kaons from D-meson decays assuming the VTX detector (a) with no p_T restriction and (b) with p_T >1.3 GeV/c. The plots were obtained using the STAR full Monte Carlo and reconstruction chain for 850 HIJING central AuAu events.

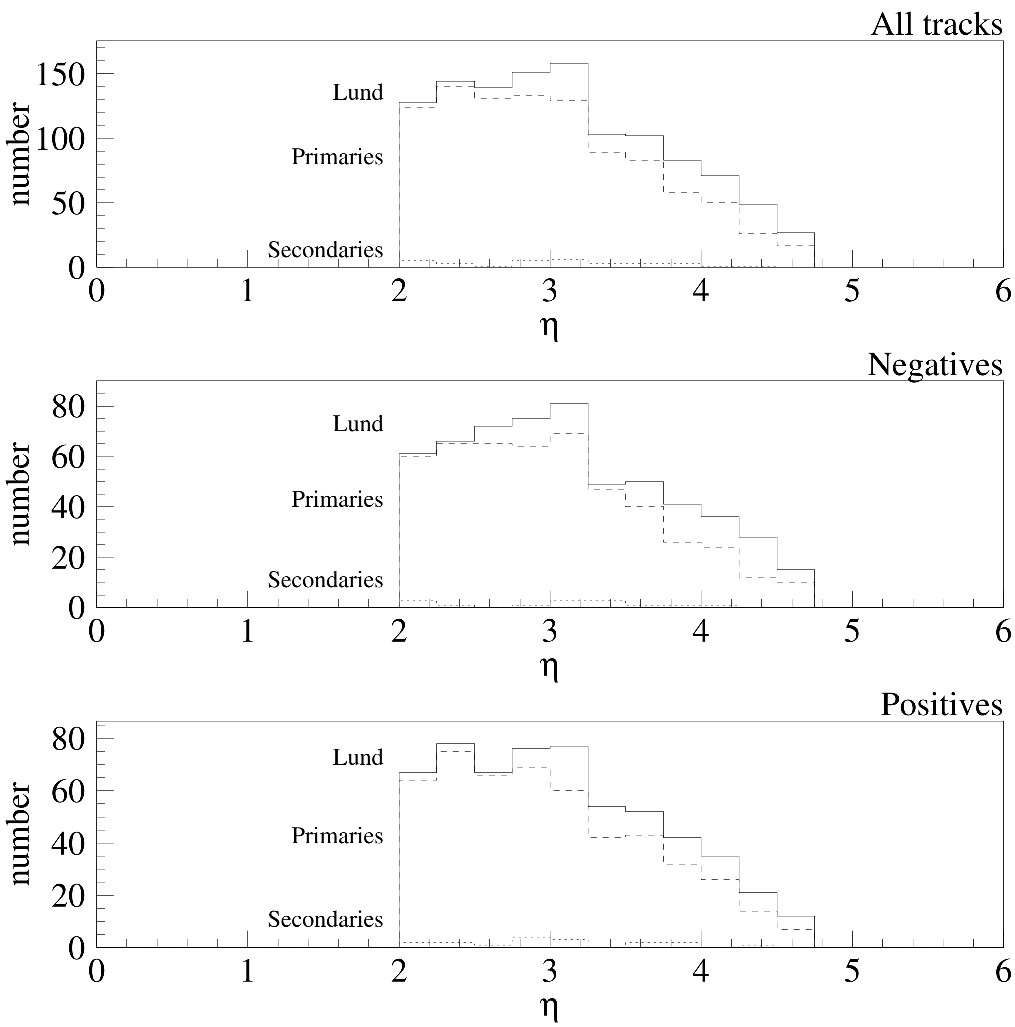

Figure 40: The $dN/d\eta$ distributions from a single event as measured by the XTPC. Included in all panels are curves for the LUND input, the reconstructed primaries and the reconstructed secondaries. The top panel includes all particles, while the middle and bottom panels are restricted to negative and positive particles, respectively. The tracker algorithm has greatly reduced the number of secondaries.

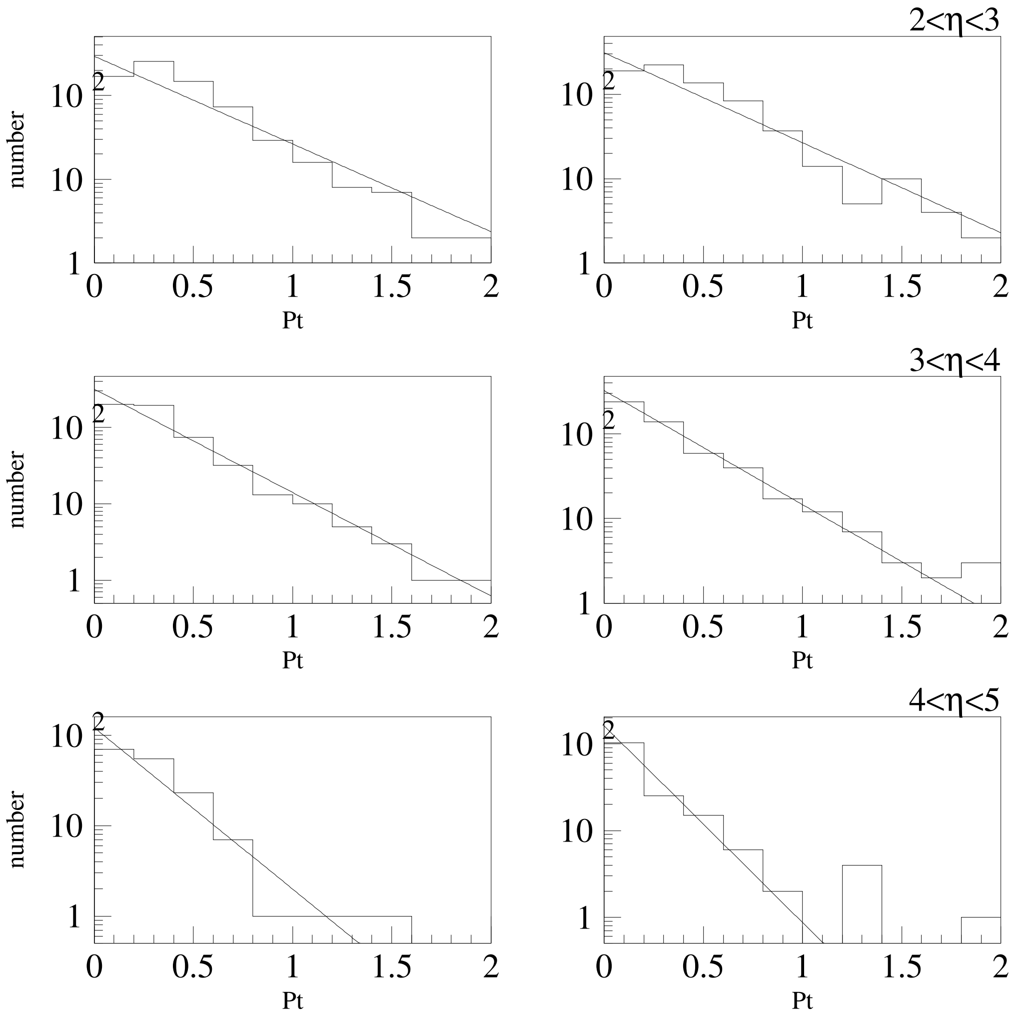

Figure 41: The p_T spectra from a single event. The panels on the left are the LUND input, while those on the right are the reconstructed tracks. From top to bottom the panels are cut on η from 2-3, 3-4, and 4-5, respectively.

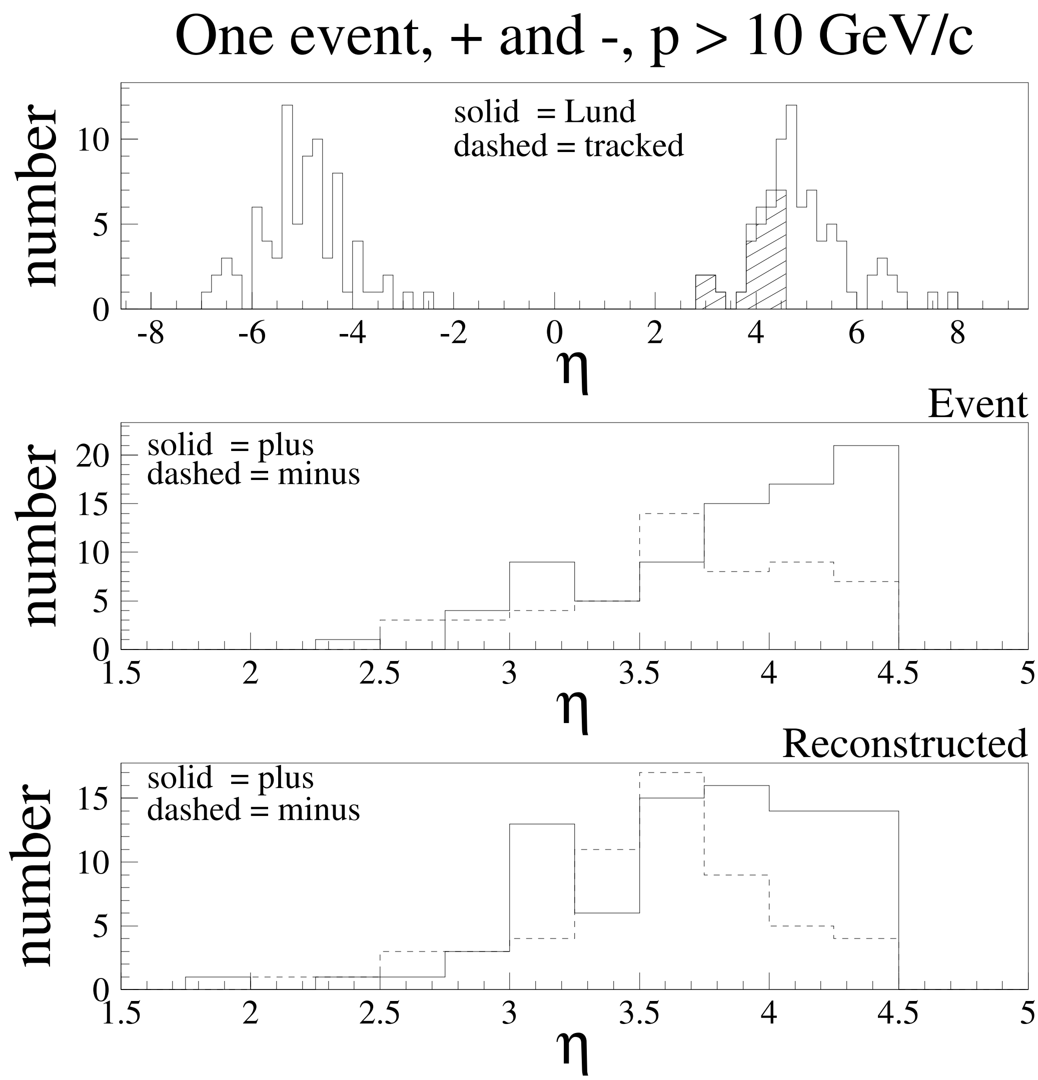

Figure 42: Charge from a single event. The top panel displays the η distribution of protons with momenta greater than 10 GeV/c predicted by the LUND model. Also shown are the fraction of those protons which are incident on the XTPC, and those which are tracked. The middle panel displays η distributions of all positively and negatively charged particles of momentum greater than 10 GeV/c predicted by the LUND model. The bottom panel displays the η distributions of reconstructed tracks separated by measured charge and gated on measured momentum above 10 GeV/c.

The contribution of Jim Draper, which is presented earlier in this document, details the XTPC's technical capabilities, *i.e.* how well the particles can be tracked, and characterized with respect to η, momentum, and charge. This paper addresses what one can learn with such capabilities.

Results

The amount of *stopping* which is generated during the course of a central relativistic heavy ion collision is the subject of many studies, both theoretical and experimental. There are wide discrepancies between models predicting the nature of heavy-ion reactions at RHIC energies. Stopping affects the other characteristics of an event, such as the $dN/d\eta$ distributions of charged particles. In Fig. 40 we present the $dN/d\eta$ distributions for a single event. In all three panels, we present the raw input from the simulated LUND (FRITIOF) event as well as the number of tracks that are reconstructed in the XTPC from GEANT data (modified by the XTPC resolution). The reconstructed tracks are identified as either primaries or secondaries based on our tracker algorithm. The LUND primaries that are not reconstructed were lost to decay, MCS, hit merging, or failures of the present tracking algorithms. Most of the secondary tracks have already been eliminated by the tracker algorithm. It is obvious that secondaries do not significantly affect the measured distribution for the XTPC system. However, the pixel detectors of PHOBOS have presented results suggesting that they too could satisfactorily measure the same distributions. In the lower two panels of the figure, we present the $dN/d\eta$ distributions separated by charge. This measurement would not be accessible to a pixel detector.

The XTPC also has the ability to measure the momentum of each track. Even if the resolution is not extremely high, statistical quantities can be studied, such as the temperatures as measured using the slope parameters of the p_T spectra. In Fig. 41, we present the p_T spectra from a single event for both the LUND input (left hand side) and the reconstructed results (right hand side). The η cuts for each pair of panels are shown. One observes that the slopes of the reconstructed spectra are within 10% of those of the input spectra. One also observes that the spectra show a hotter temperature for the more mid-rapidity η region. One expects the mid-rapidity region to be the hottest, but the ability to **quantify** the temperatures of different regions within a single event is a character unique to STAR (neither PHOBOS nor BRAHMS can make such a measurement).

The most forward regions at RHIC are not only characterized as *colder* than the central regions, but they are also expected to have a higher baryon density. The 'spectator' protons will appear in the high η regions. From these protons we can learn about the nature of the collision. The stopping that occurred during the collision should be directly measureable from the $dN/d\eta$ distribution of the spectator protons. However, it is not possible to identify whether a given proton was created during the collision or was present in one of the colliding nuclei. Indeed, at $\eta > 2$ it is extremely difficult even to determine the particle species. BRAHMS can accurately determine the particle identification and momentum, but they can only do this over an extremely narrow acceptance (in η and ϕ) in a given event. The XTPCs can study the residual positive charge distribution to infer the nature of the spectator proton distribution. Fig. 42 indicates the present degree to which the XTPCs are able to achieve this goal on an event-by-event basis. The top panel displays the primary proton η distribution from LUND. These protons are cut on momenta greater than 10 GeV/c. This minimizes the created protons and leaves distributions suggestive of the disassembly of the projectile nuclei. Also shown on the right hand side of the top panel is an indication of the protons which would be incident on the XTPCs and successfully tracked (losses are due to interactions in intervening material). The middle panel displays the η distribution of all the primaries from LUND for positive and negative charges with $p > 10$ GeV/c. The difference between these two spectra is a *measurable* quantity for the XTPC. This difference between the positive and negative spectra fairly resembles the proton distribution for this event. The final panel displays the positive and negative η distributions that would be measured in the XTPC for this event. One observes that the signal is still measureable and can be improved with a better tracking algorithm. Thus one can do event-by-event measurements of the residual charge excess, and this quantity does relate to the spectator proton distribution. The ability to characterize the excess positive charge distribution on an event-by-event basis gives STAR a powerful tool for cross-correlating information. PHOBOS and BRAHMS do not have this capability.

The author would like to recognize those who **actually** did the work: Jim Draper, Lynn Wood, and Juan Romero. This work was supported by the National Science Foundation under contract number PHY-91-23301.

3.5 Pion Interferometry at STAR

Contributed by: Sanjeev U. Pandey

Introduction

Two-particle intensity interferometry provides a method for measuring the space–time extent of a particle-emitting source when the emitted radiation is at least partially incoherent. Intensity interferometry measures the freeze-out volume when the particles decouple from the source and recently is thought to shed light on the measurement of flow. The aim of this work is to determine what are the present HBT capabilities of the STAR detector (TPC + SVT), in particular with regard to the maximum source size we can measure and with regard to single event HBT. This section also addresses how each of these can be improved.

Method

The event generator used here is the pion laser HIJET code developed by R. Longacre which has Bose-Einstein correlations built in as well as two particle Coulomb repulsions. Many events were generated for source sizes of 7 fm, 15 fm and 21 fm; the output consisted of lists of momentum vectors tagged with particle type. The events were simulated in STAR with GEANT and analyzed using the full tracking chain including SVT and TPC tracking, SVT-TPC track matching, global track refitting, PID using dE/dx in the SVT and TPC, and track extrapolation to the vertex with the final set of reconstructed tracks being listed in the TAS table PARTICLE from which correlations in momentum space were computed. These correlations were corrected for Coulomb repulsion using the Gamov factor. Residual background, momentum resolution, and pair acceptance corrections were not applied. Poisson based maximum likelihood fits were performed and compared to correlations formed from the input distributions.

Realistic tracking, PID, Coulomb biases, and symmetrized events are what distinguish this study from others. However, these events have about 4 times as many particles as usual HIJING events and thus are more sensitive to tracking problems.

Some Issues

One is interested in measuring accurately the sigma of a Gaussian which is proportional to $1/Radius$. With a momentum resolution of 10 MeV/c the maximum source size one can expect to measure is set by this scale and is about 20-25 fm (rms), the lower estimate arising from demanding at least 4 points in the peak. Further, resonances distort the pion correlation precisely in the first 10-15 MeV/c of the correlation where the 20 fm signal is dominant. Single event HBT on the other hand is limited by statistics in the low Q area and thus depends on dN/dy which is ill determined at present. Both of these estimates depend crucially on two-track separation efficiency. Present tracking algorithms do not address deconvolution of nearby or merged tracks. Further problems which affect correlation studies are track fragmentation (*i.e.,* at low p_T single tracks in the TPC are often

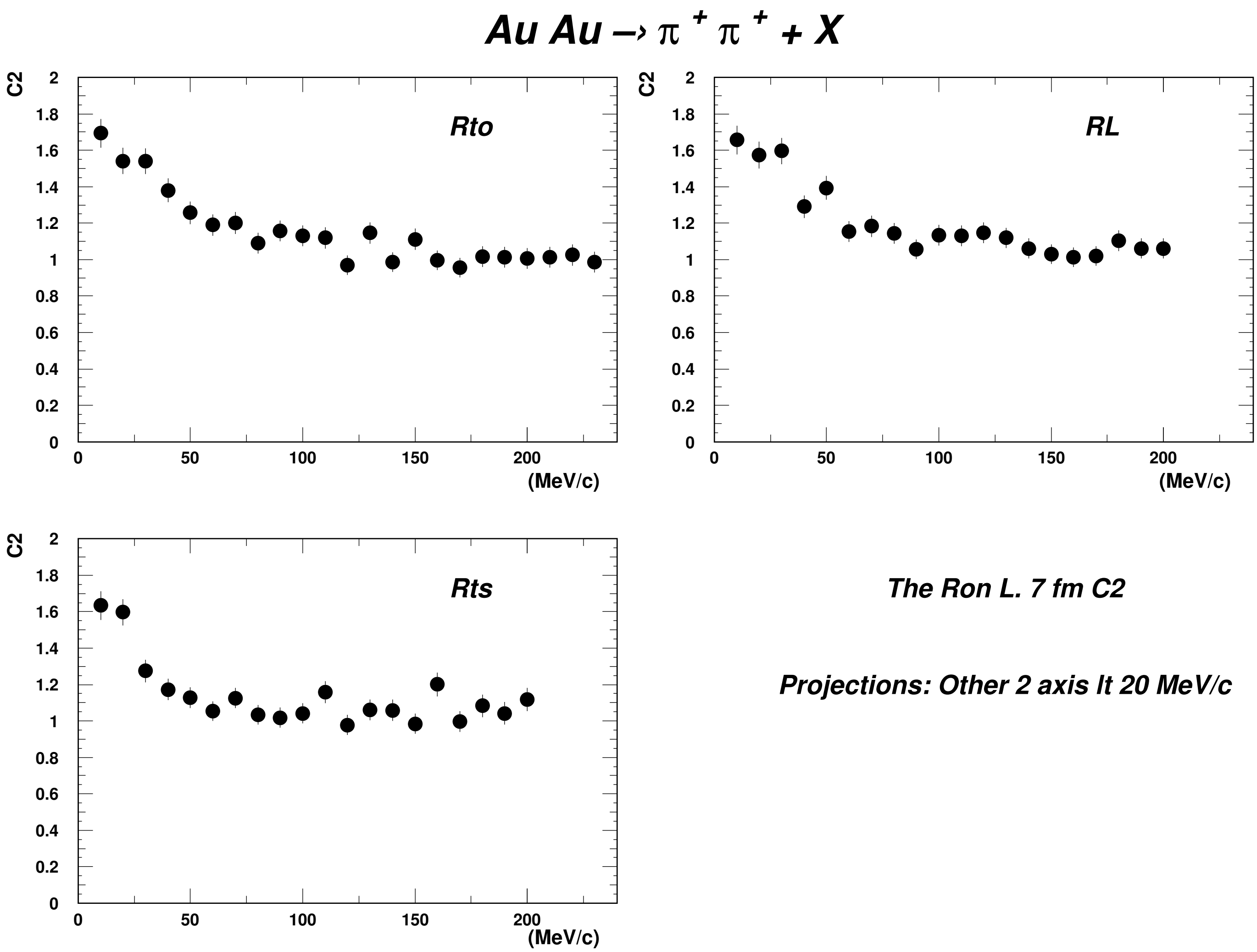

Figure 43: HBT figure.

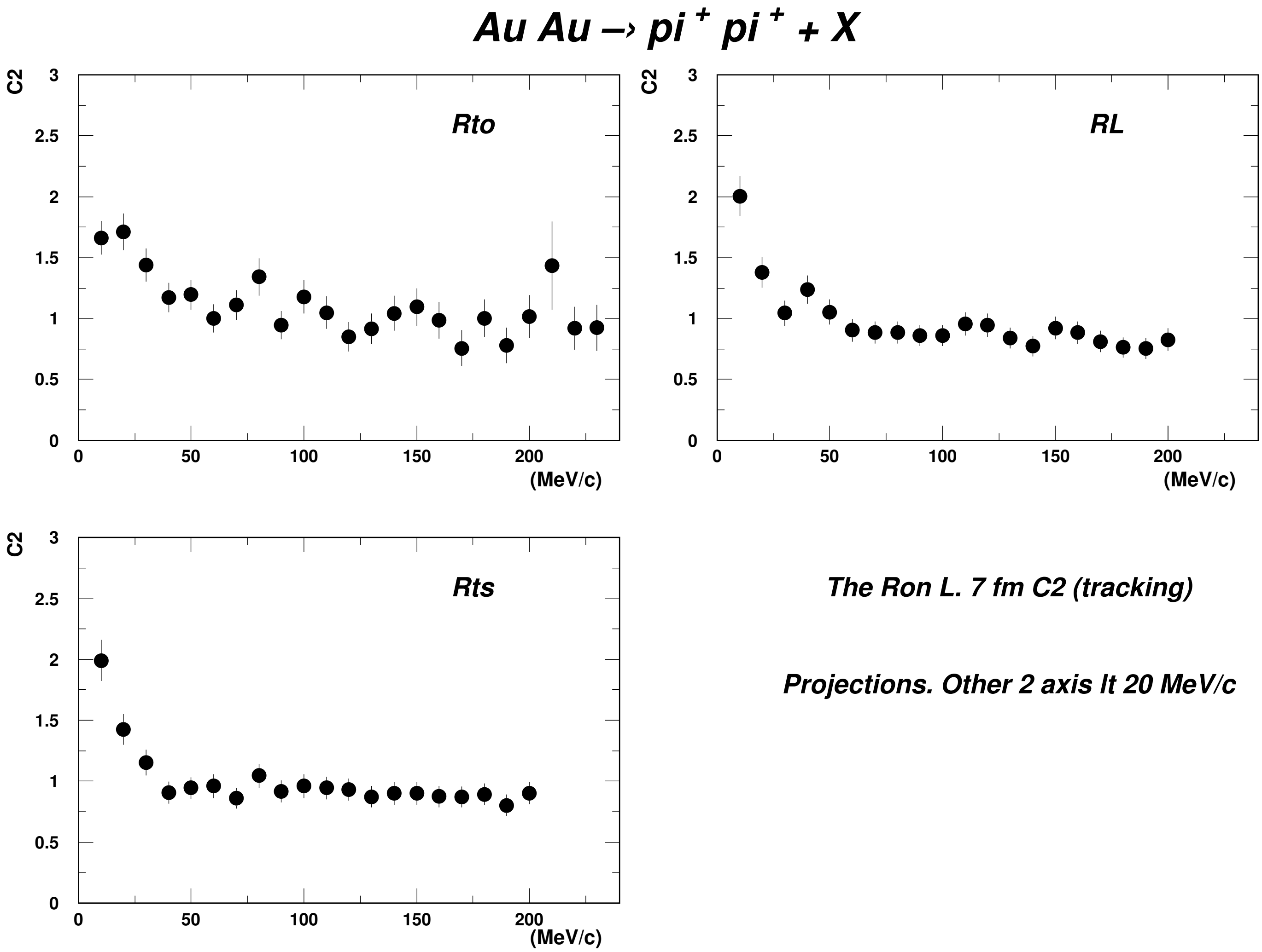

Figure 44: HBT figure.

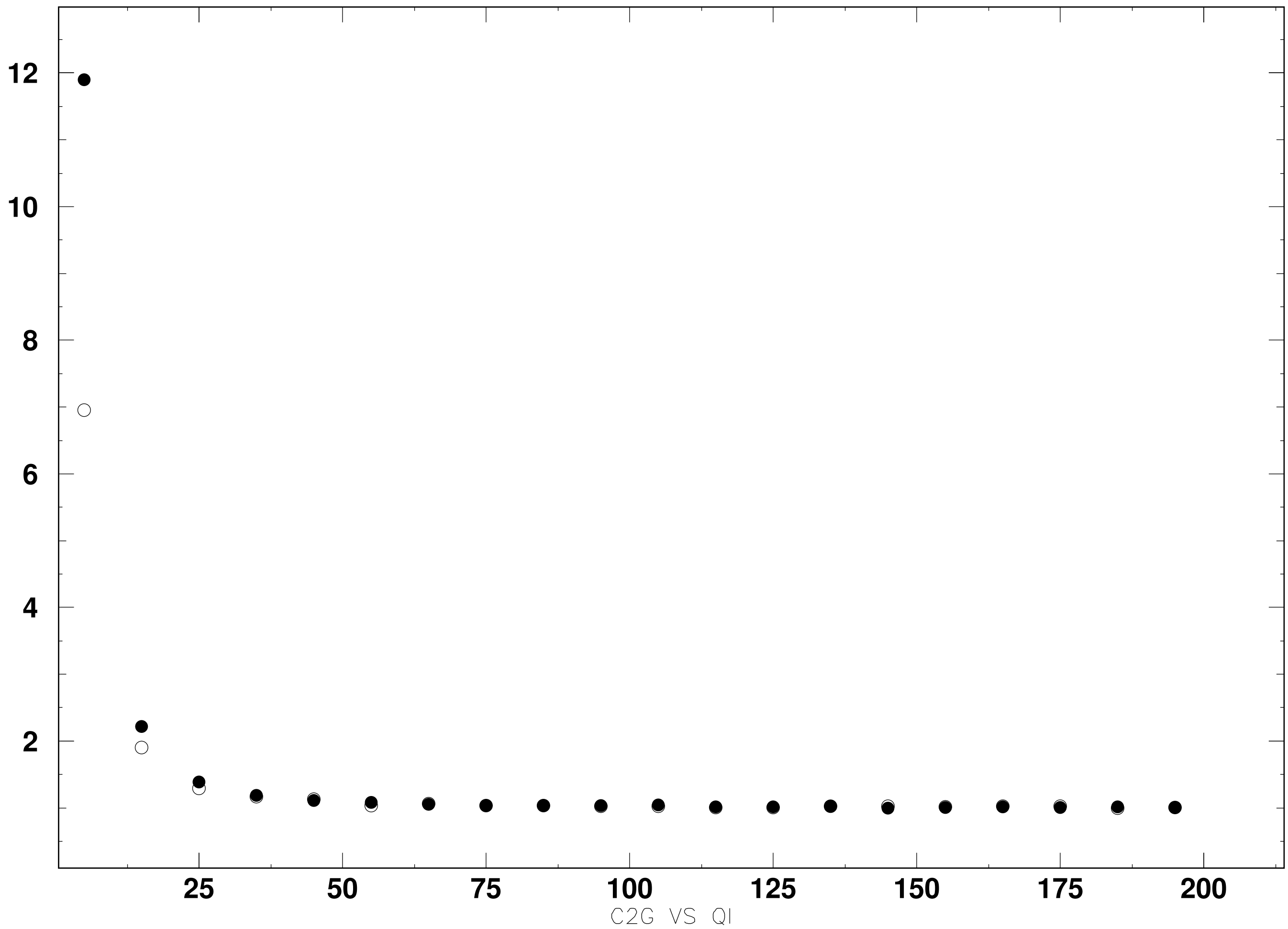

Figure 45: HBT figure.

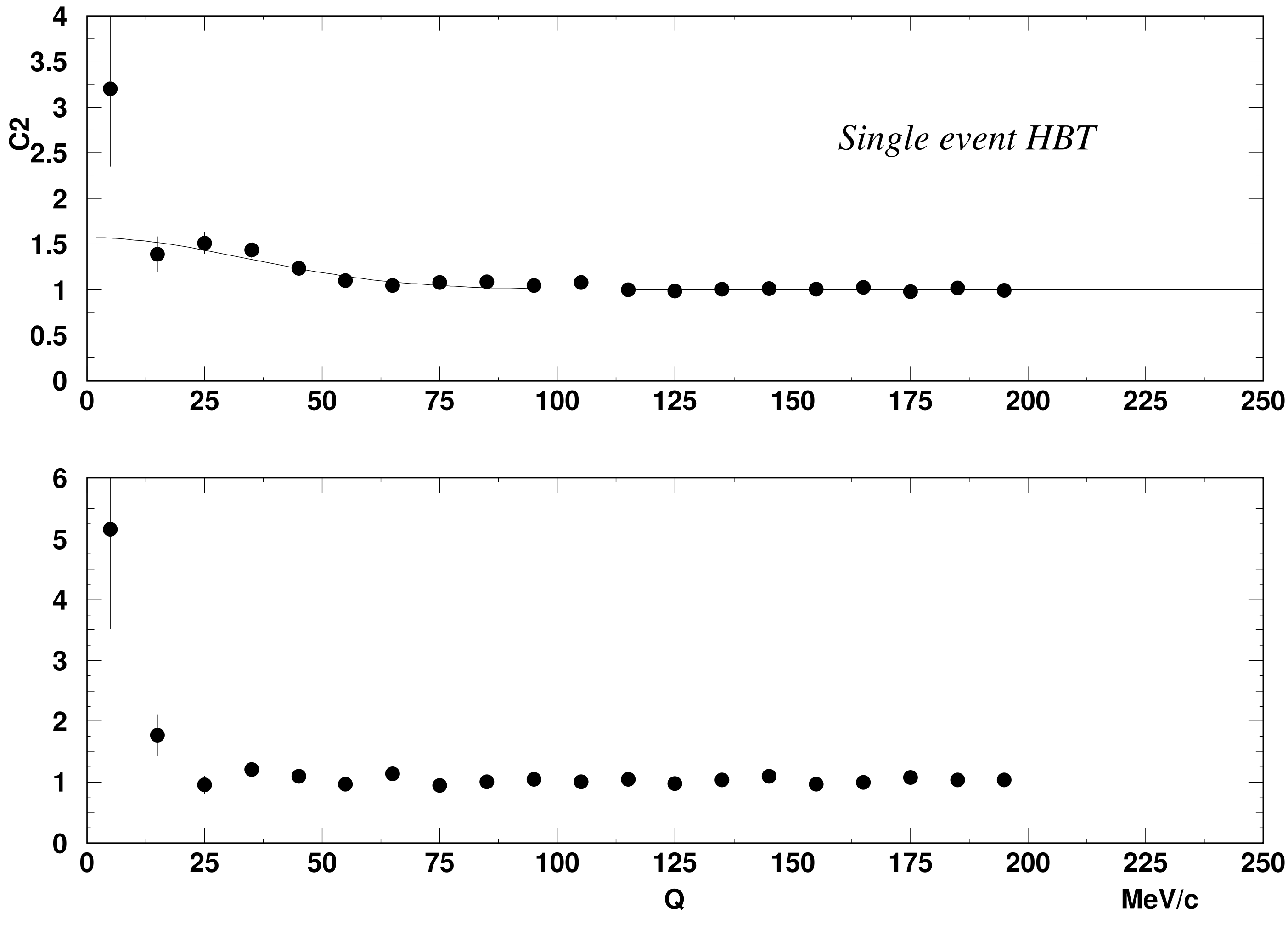

Figure 46: HBT figure.

broken into fragments, each being mistaken for a different track with very similar momentum) and tracking errors in the SVT which result when one particle produces hits on two overlapping wafers in the innermost layer of the SVT. Both of these effectively create fake correlations which have to be minimized.

Results

The three projections (out, side and longitudinal) of the input 7 fm 3D correlation for 10 events are shown in Fig. 43; Fig. 44 shows the corresponding correlations after passing through the STAR detector and the event reconstruction analysis chain. In this model the source is symmetric ($R_{ts} = R_{to} = R_L$). Correlation function fits to the input and output distributions lead to similar results. However, the reconstructed correlation functions display large fluctuations. Projections hide information and Fig. 45 can help one understand the problem. Shown in Fig. 45 is a correlation in Q_{inv} for a 15 fm source for 10 events after passing through the STAR detector. The solid dots are with no cuts and the open circles are with a $p_T > 200$ MeV/c cut which reduces the huge spurious peak at low Q. This cut is effective in reducing the number of ghost tracks. Further cuts which can be applied to the data to enhance purity are to require $y < 1$, long fragment lengths, minimum double hit separations, etc. While a 15 fm source size can still be extracted from fits to this correlation function one sees that HBT is very sensitive to track purity issues.

Finally Fig. 46 shows the single event HBT capabilities of the STAR detector at the present stage of our analysis chain. The top part is for a 7 fm source and the bottom part is for a 15 fm source; both are derived after the $p_T > 200$ MeV/c cut. There are about 900 pions in the event. This is a resonable number since it spans 4 units of rapidity and in the final analysis it is envisioned to mix π^+ and π^- together. While the 7 fm source is well fit with 50% errors, the 15 fm source cannot be fit at the present time without cleaning up the previously mentioned tracking errors. As an aside one should mention that while single event HBT can only be done in 1D, since R_{inv} is proportional to R_{ts} this is not a huge drawback. In addition no binning fits are being investigated to reduce statistic problems.

Conclusions

At present STAR HBT capabilities are limited by tracking purity issues rather than by momentum resolution or dN/dy. With the present analysis software one can measure a maximum source size of 15 fm (rms) and a maximum single event HBT size of 7 fm (rms). These numbers should improve in the future with better tracking. However, a whole slew of other problems might complicate interpretations (*e.g.* $r - p$ correlations, resonances, Coulomb effects, ...) and thus more work needs to be done in this area.

I am very grateful to Lanny Ray and Ron Longacre without whom none of the above would have been possible.

4 Cumulative References

References

[1] P. Jones and I. Sakrejda, STAR-Note 0056.

[2] W.G. Gong, Starnote (in preparation).

[3] R.J. Morse, LBL-35768, p.140, 1994.

[4] M.J. LeVine and D. Rohrich, proceedings of the STAR collaboration meeting (Jan. 1992).

[5] H. Wieman, private communication.

[6] S. Ahmad, B. E. Bonner, W. Gere, G. S. Mutchler, P. Rambo, S. Toshkov, E. Platner, H. J. Crawford and J. M. Engelage, Nucl. Inst. Meth. **A 330**, 416 (1993).

[7] J. Draper, L. Wood, J. Romero, D. Cebra, and Brady, "Realistic Analytical Model of XTPC Performance; Reconstruction; Secondary Rejection," Starnote 187, Jan. 1995.

[8] M. Gyulassy, Nucl. Phys. **A400**, 31c (1985); L. Van Hove, Z. Phys. **C27**, 135 (1985).

[9] J. D. Bjorken, Int. J. Mod. Phys. A **7**, 4189 (1992).

[10] B. Nilsson-Almqvist and E. Stenlund, Comp. Phys. Comm. **43**, 387 (1987).

[11] GEANT version 3.15.

[12] E. Schnedermann, NATO ASI Series **B303**.

[13] S. Gavin, "Disoriented Chiral Condensates," invited talk presented at Quark Matter '95, Monterey, CA, (Jan., 1995), to be published.

[14] *The STAR Collaboration*, Conceptual Design Report for the Solenoidal Tracker at RHIC (STAR), June 15, 1992.

[15] *The STAR EMC Collaboration*, Conceptual Design Report for the Electromagnetic Calorimeter for the **STAR**, September 22, 1993.

[16] Miklos Gyulassy and Xin-Nian Wang, LBL-34246 (1994).

[17] T. Sjostrand, CERN-TH. 7112/93 (1993).

[18] Arnison *et al.*, (UA1 Collaboration), Phys. Lett. **132B**, 214 (1983).

[19] B. Flaugher and K. Meier, FERMILAB-Conf-90/248-E, 1990.

[20] V. Korotkikh *et al.*, Preprint INP MSU 94-30/352, 1994.

[21] Arnison *et al.*, (UA1 collaboration), Phys. Lett. **132B**, 223 (1983).

[22] For an analysis of $(1/m_T)dn/dm_T$ data to extract temperatures and flow velocities see, e.g. E. Schnedermann, J. Sollfrank and U. Heinz, Phys. Rev. **C 48** (1993) 2463.

[23] J.Boltz *et al.*, Phys. Lett. **B 300** (1993) 404.

[24] S.Pratt *et al.*, Phys. Rev. Lett. **68** (1992) 1109.

[25] S.Uddin and C.P. Singh, Phys. Lett. **B 278** (1992) 357.

[26] R.D. Pisarski and F. Wilczek, Phys. Rev. **D 29** (1984) 338; T. Hatsuda and T. Kunihiro, Phys. Lett. **B 185** (1987) 304; E.V. Shuryak, Nucl. Phys **A 525** (1991) 3c.

[27] M. Asakawa, C.M. Ko (Texas A-M), 1994. Nucl. Phys. **A 572** (1994) 732.

[28] Y. Wang *et al.*, "Multiplicity Dependence of the Mass of the ϕ-meson from Si+Au Collisions at 14.6 GeV/c," in *Quark Matter '95*, January 95, (California).

[29] X.-N. Wang, to be published, private communication.

[30] X.-N. Wang and M. Gyulassy, Phys. Rev. **D 44** (1991) 3501.

[31] W.Geist, Phys. Lett. **B 211** (1989) 233.

[32] S.Gavin *et al.*, Phys. Lett. **B 234** (1990) 175.